Contrib Mineral Petrol (2013) 165:217–236
DOI 10.1007/s00410-012-0806-9

ORIGINAL PAPER

Chalcophile element geochemistry of the Boggy Plain zoned pluton, southeastern Australia: a S-saturated barren compositionally diverse magmatic system

Jung-Woo Park · Ian H. Campbell · Ryan B. Ickert · Charlotte M. Allen

Received: 27 May 2012 / Accepted: 27 August 2012 / Published online: 13 September 2012

Abstract The behavior of the platinum group elements (PGE) and Re in felsic magmas is poorly understood due to scarcity of data. We report the concentrations of Ni, Cu, Re, and PGE in the compositionally diverse Boggy Plain zoned pluton (BPZP), which shows a variation of rock type from gabbro through granodiorite and granite to aplite with a SiO_2 range from 52 to 74 wt %. In addition, major silicate and oxide minerals were analyzed for Ni, Cu, and Re, and a systematic sulfide study was carried out to investigate the role of silicate, oxide, and sulfide minerals on chalcophile element geochemistry of the BPZP. Mass balance calculation shows that the whole rock Cu budget hosted by silicate and oxide minerals is <13 wt % and that Cu is dominantly located in sulfide phases, whereas most of the whole rock Ni budget (>70 wt %) is held in major silicate and oxide minerals. Rhenium is dominantly hosted by magnetite and ilmenite. Ovoid-shaped sulfide blebs occur at the boundary between pyroxene phenocrysts and neighboring interstitial phases or within interstitial minerals in the gabbro and the granodiorite. The blebs are composed of pyrrhotite, pyrite, chalcopyrite, and S-bearing Fe-oxide, which contain total trace metals (Co, Ni, Cu, Ag, Pb) up to ~16 wt %. The mineral assemblage, occurrence, shape, and composition of the sulfide blebs are a typical of magmatic sulfide. PGE concentrations in the BPZP vary by more than two orders of magnitude from gabbro (2.7–7.8 ppb Pd, 0.025–0.116 ppb Ir) to aplite (0.05 ppb Pd, 0.001 ppb Ir). Nickel, Cu, Re, and PGE concentrations are positively correlated with MgO in all the rock types although there is a clear discontinuity between the granodiorite and the granite in the trends for Ni, Rh, and Ir when plotted against MgO. Cu/Pd values gradually increase from 6,100 to 52,600 as the MgO content decreases. The sulfide petrology and chalcophile element geochemistry of the BPZP show that sulfide saturation occurred in the late gabbroic stage of magma differentiation. Segregation and distribution of these sulfide blebs controlled Cu and PGE variations within the BPZP rocks although the magma of each rock type may have experienced a different magma evolution history in terms of crustal assimilation and crystal fractionation. The sulfide melt locked in the cumulate rocks must have sequestered a significant portion of the chalcophile elements, which restricted the availability of these metals to magmatic-hydrothermal ore fluids. Therefore, we suggest that the roof rocks that overlay the BPZP were not prospective for magmatic-hydrothermal Cu, Au, or Cu–Au deposits.

Keywords Platinum group elements · Chalcophile elements · Gabbro · Granite · Sulfide saturation · Magmatic sulfide bleb · Boggy Plain zoned pluton

Communicated by J. Hoefs.

Electronic supplementary material The online version of this article (doi:10.1007/s00410-012-0806-9) contains supplementary material, which is available to authorized users.

J.-W. Park (✉) · I. H. Campbell · R. B. Ickert · C. M. Allen
Research School of Earth Sciences, The Australian National University, Canberra, ACT 0200, Australia
e-mail: jung.park@anu.edu.au

R. B. Ickert
Berkeley Geochronology Center, 2455 Ridge Road, Berkeley, CA 94709, USA

Introduction

There is a well-known correlation between felsic igneous intrusions and granite-related ore deposits such as Cu, Au,

or Cu–Au porphyry, skarn, and other magmatic-hydrothermal deposits (Candela 1997), but not all felsic intrusions are associated with mineralization. Why some felsic intrusions are linked to these deposits whereas others are not is poorly understood. A possible explanation is that barren felsic systems become saturated with an immiscible sulfide melt and precipitate and crystallized that melt before the host magma becomes volatile saturated. If this occurs, most of the Cu and Au will be locked in a dispersed sub-economic sulfide phase within a subvolcanic magma chamber and the metals will be unavailable to form a more concentrated magmatic-hydrothermal Cu–Au deposit. In contrast, if the evolving felsic melt becomes volatile saturated before it becomes sulfide-saturated, most of the Cu and Au in the system will be available to enter any magmatic-hydrothermal fluid emanating from the intrusion, which may lead to the formation of an economic Cu, Au, or Cu–Au deposits, depending on the composition of the hydrothermal fluid and the availability of a suitable trap. Alternatively, if a melt becomes sulfate saturated, the metals will still be available to ore-forming fluid because Cu and Au do not partition strongly into the precipitating sulfate phase. Note that felsic intrusions associated with Cu, Au, or Cu–Au mineralization are commonly highly oxidized (Robb 2004) and sulfur will dissolve in a highly oxidized magma as sulfate species (Carroll and Rutherford 1985; Jugo 2009).

Given the argument above, identifying sulfide saturation in an evolving felsic system is a key to understanding the geochemistry of chalcophile elements such as Cu and Au and the potential for economic Cu–Au mineralization. Identifying the onset of sulfide saturation could be accomplished by direct analyses of Cu and Au, but the advantage of studying the platinum group elements (PGE) is that they have much higher partition coefficients in immiscible sulfide melts than Cu and Au (Francis 1990; Bezmen et al. 1994; Crocket et al. 1997; Ripley et al. 2002; Fonseca et al. 2009) and are therefore more sensitive indicators of sulfide saturation. In addition, the PGE are less mobile during hydrothermal alteration than Cu and Au (e.g., Crocket 2000). Mobility of Cu and Au in the altered rocks associated with Cu, Au, or Cu–Au mineralization often leads to erratic data that are difficult to interpret.

Despite the significance of PGE geochemistry of felsic igneous rocks, it is poorly constrained due to lack of data (e.g., Setiabudi et al. 2007). In this study, we analyzed the Boggy Plain zoned pluton (BPZP) as a first step toward understanding the fundamental geochemistry of the PGE in a felsic magmatic system. The BPZP is one of the most studied igneous suites in the Lachlan Fold Belt (Wyborn 1983; Wyborn et al. 1987, 2001; Hoskin 2000; Hoskin et al. 2000; Ickert 2010; Ickert et al. 2011) so that its petrogenesis is well documented. This pluton shows large compositional variation from olivine-bearing two-pyroxene gabbro to granite and aplite with SiO_2 range of 52–74 wt %, which provides a good opportunity to observe chalcophile element and PGE behavior during magma differentiation from mafic to felsic rocks. Wyborn (1983) and Ickert et al. (2011) provided major element, some trace element, isotope and modal abundance data for the BPZP and these data form the background to this study. Here, we present whole rock PGE, Re and additional trace element data as well as analyses of chalcophile elements in silicate and oxide minerals, using the same set of samples as Wyborn (1983) and Ickert et al. (2011). We also carried out a systematic study of the sulfides in the BPZP rocks using optical microscopy and electron microprobe data. We compiled all these datasets to investigate the chalcophile elements and PGE behavior in a compositionally diverse suite to address role of silicate, oxide, and sulfide mineral fractionation on the geochemistry of the chalcophile elements and PGE. The results have implications for distinguishing barren from productive felsic magmatic systems.

Geological and petrological background

The BPZP is located in the most northern part of the Kosciuszko Batholith in the Lachlan Fold belt, southeastern Australia (Fig. 1). It intrudes the early Silurian Gang Gang quartz monzonite and the middle Ordovician Boltons Beds that are composed of graywackes and shales (Wyborn 1983). SHRIMP U–Pb zircon analyses give the crystallization age of the BPZP as 417 ± 2.0 Ma (Ickert et al. 2011). This early Devonian period is associated with the development of rift basins in a back-arc setting (Glen 2005). The parental magma of the BPZP is interpreted to have formed by decompression melting of metasomatized upper mantle (Ickert 2010). The Boggy Plain Fault, a north–south trending strike-slip fault, dissects the BPZP, which displaces the western part of the pluton about 5 km south of the eastern part (Wyborn 1983). The BPZP is a relatively dry and high temperature system, which crystallizes anhydrous minerals such as plagioclase and pyroxene as the early crystallizing phases (Wyborn et al. 2001). Two-pyroxene geothermometry on gabbroic rocks in the BPZP yields temperature of 900–1050 °C, and contact metamorphic phase reactions constrain the lithostatic pressure at between 2.5 and 3.0 kbar (Wyborn 1983; Ickert et al. 2011).

The BPZP shows a great diversity of rock types ranging from two-pyroxene gabbro to aplite with a SiO_2 range of 52–74 wt % and a MgO range of 7.6–0.53 wt % (Wyborn 1983). The rocks are concentrically distributed to form a zoned bull's-eye shaped intrusion with the gabbro at the margin followed by granodiorite then granite and finally

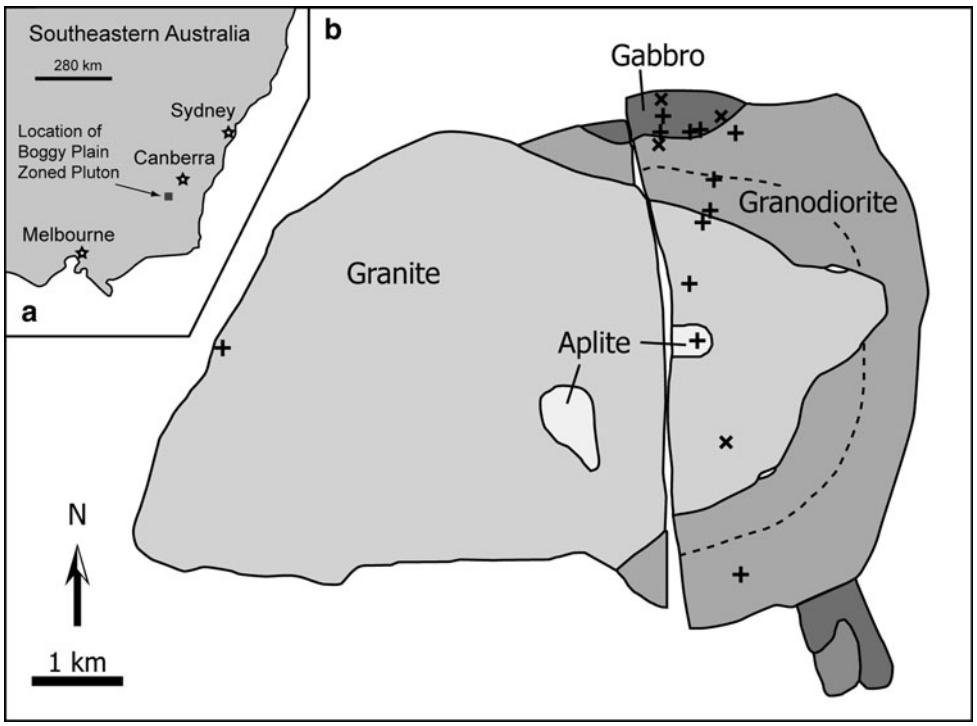

Fig. 1 **a** Location of the BPZP in southeastern Australia. **b** Simplified geological map of the BPZP showing locations of the samples analyzed for PGE (*plus symbols*) and for mass balance only (*negative crosses*). Detailed information on the sample sites is given in Wyborn (1983) and Ickert et al. (2011). The *dashed line* divides the outer and inner granodiorite based on the sum of MgO and total FeO contents (after Wyborn et al. 2001). Note that ~5 km of left-lateral movement along the Boggy Plain Fault is restored. Both maps modified from Wyborn (1983) and Ickert et al. (2011)

aplite near the center (Fig. 1). The gabbro–granodiorite contact is gradual, whereas the granodiorite–granite contact is sharp and discordant (Wyborn 1983). The granite–aplite contact is not exposed, but is considered to be sharp (Wyborn 1983).

The gabbro consists mainly of euhedral plagioclase, orthopyroxene, and clinopyroxene with interstitial quartz, biotite, hornblende, and minor orthoclase and olivine (Wyborn 1983). Most clinopyroxene crystals are rimmed by hornblende. The modal abundance of interstitial hornblende, biotite, and quartz in the gabbro varies between 14 and 34 modal % (Wyborn 1983). The granodiorite contains clinopyroxene and strongly zoned plagioclase as major mineral phases with interstitial minor hornblende, quartz, orthoclase, and biotite (Wyborn 1983). They can be divided into a pyroxene-rich outer granodiorite and a plagioclase-rich inner granodiorite (Wyborn 1983). Euhedral hornblende, biotite, and plagioclase are the major phases in the granite with clinopyroxene as a minor phase. The aplite consists mainly of quartz, orthoclase, plagioclase, and biotite (Wyborn 1983).

Hoskin et al. (2000) studied accessory minerals in the BPZP in detail. Zircon, apatite, and magnetite occur in all rock types of the BPZP, and allanite and titanite are present in all rock types except the gabbro. Ilmenite is present in the gabbro and granodiorite, but the abundance decreases in the granodiorite. Ickert et al. (2011) recently studied zircons of the BPZP and measured zircon crystallization temperatures using the Ti-in-zircon thermometry. They reported similar crystallization temperatures of 750–850 °C for all rock types despite different zircon morphologies and the wide variation in bulk rock compositions.

Wyborn (1983) and Wyborn et al. (2001) attributed the wide range in compositional variation of the BPZP to convective fractionation process in a closed system. They suggested that crystallization began at the margin of the magma chamber, forming the gabbro and granodiorite as pyroxene- and plagioclase-rich cumulates from a high temperature homogeneous parental magma accompanied by convective separation of the residual melt which accumulates in the center of the intrusion to form the granite and aplite. However, a recent isotope study by Ickert (2010) revealed that each phase of the BPZP is derived from compositionally similar, but isotopically different parental magmas. The zircon $\delta^{18}O$ values are ~5.5 ‰ for gabbro and ~6.5 ‰ for the remaining rock types, indicating 10–20 % of crustal assimilation in the magmas from which the granodiorite, the granite, and the aplite crystallized (Ickert 2010; Ickert et al. 2011). The BPZP also shows a complex pattern of zircon εHf_i and whole rock εNd_i data variations. The gabbro ($\varepsilon Hf_i = +3.2$, $\varepsilon Nd_i = +0.72$) and inner granodiorite ($\varepsilon Hf_i = +2.2$ to $+2.4$, $\varepsilon Nd_i = +1.39$ to $+2.49$) are more juvenile than outer granodiorite ($\varepsilon Hf_i = -2.5$, $\varepsilon Nd_i = -0.62$), granite ($\varepsilon Hf_i = -1.7$ to -2.3, $\varepsilon Nd_i = -0.63$ to -0.99), and aplite ($\varepsilon Hf_i = -1.0$, $\varepsilon Nd_i = -1.46$), which have assimilated a higher fraction of crustal material (Ickert 2010).

Analytical techniques

Mineral analysis

Analyses of the major silicate and oxide minerals from the BPZP were carried out on polished thin sections. Major element compositions for selected orthopyroxene, clinopyroxene, biotite, hornblende, plagioclase, magnetite, and ilmenite were analyzed using a JEOL6400 scanning electron microscope (SEM) in energy-dispersion X-ray spectrometer (EDS) mode at the Australian National University (ANU) with beam conditions of 15 kV and 20 nA. Trace element concentrations in the silicate and oxide minerals were then determined by laser ablation (LA)-ICP-MS at the Research School of Earth Sciences (RSES), at the ANU. This system consists of a Lambda Physik Complex 110 excimer laser ($\lambda = 193$ nm) and an ANU-designed HelEx ablation cell, coupled to an Agilent 7500 ICP-MS or Agilent 7700 ICP-MS, with He as the laser ablation carrier gas. LA-ICP-MS analyses were performed using a laser pulse rate of 5 Hz and spot sizes that varied between 62 and 102 μm. Each analysis consisted of 30 s of background measurement followed by 40 s of sample ablation. A NIST 612 glass standard was used as the external standard with Si obtained from electron microprobe analyses (EPMA) employed as the internal standard for silicate minerals, except where indicated below. A NIST 610 glass standard was used for magnetite and ilmenite with Fe obtained from EPMA. Silicon contents in plagioclase were calculated using LA-ICP-MS data based on stoichiometry with assumption that the sum of SiO_2, Al_2O_3, CaO, and Na_2O is 100 wt %; this was useful for some samples for which the EPMA data were not obtained. Figure 2 shows the comparison of anorthite composition in plagioclase from BP30 and BP4 calculated using data obtained by both electron microprobe analyses and LA-ICP-MS analyses. The results agree to 15 % uncertainty, which verifies the accuracy of Si contents in plagioclase calculated using LA-ICP-MS data. The Si contents in some orthopyroxenes, clinopyroxenes, and hornblendes were assumed to be the same as the Si contents in these minerals in other mineral grains from the same rock type. Since Si contents in these minerals vary within 1.5 % regardless of sample and rock type, the uncertainty arises from this assumption is less than the analytical uncertainty of LA-ICP-MS method. Standards were analyzed before and after analyses of 5–8 unknown points. Data reduction was performed following the method of Longerich et al. (1996). The detection limits for the analyzed elements were calculated using the relationship described in Longerich et al. (1996) and Sylvester and Eggins (1997). Multiple analyses of BCR-2 g (USGS) indicate that analytical precision (1σ) is better than 5 % for all elements, except for Pb (8 %) (Electronic supplementary materials). Our measured value for BCR-2 g is consistent with the reference values from Gao et al. (2002) and GeoReM database (http://georem.mpch-mainz.gwdg.de/) within 10 % for most of the elements. The major and trace element composition of silicate and oxide minerals and BCR-2 g is provided in Electronic supplementary materials.

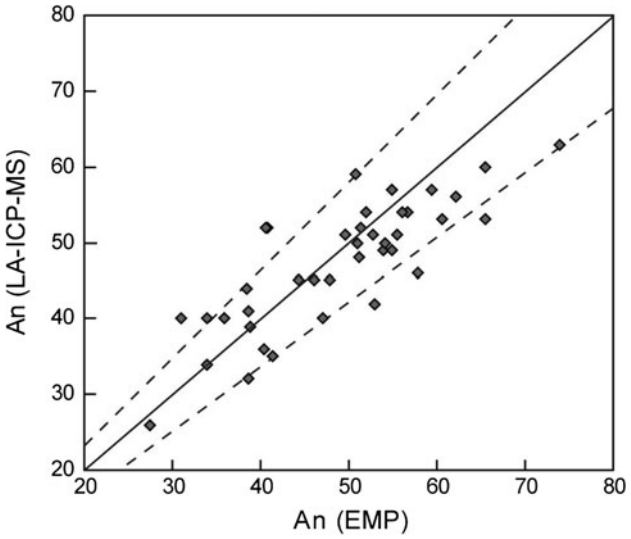

Fig. 2 Comparison of anorthite (An) composition in plagioclase obtained from EPMA and LA-ICP-MS analyses. The *solid line* represents the 1:1 ratio and the *dashed lines* represent ± 15 % uncertainty (1σ)

Magmatic sulfides from sulfide blebs and disseminated secondary sulfides were analyzed for S, Fe, Co, Ni, Cu, Zn, Ag, and Pb using polished thin sections. Sulfur-bearing Fe-oxide from sulfide blebs and Ti–Fe oxide phenocrysts were also analyzed for MgO, Al_2O_3, SiO_2, FeO, Cr_2O_3, MnO, V_2O_3, NiO, TiO_2, and SO_3. Analyses were performed by a JEOL6400 SEM in EDS mode or a CAMECA SX100 electron microprobe in WDS mode at the ANU with the beam conditions of 15 kV and 20 nA. FeO and Fe_2O_3 contents in the S-bearing Fe-oxide, magnetite, and ilmenite were calculated from charge balance and stoichiometry following the method described in Carmichael (1966).

The concentrations of Pt, Ir, Os, and Au in sulfide were determined by LA-ICP-MS at the RSES, ANU using the same LA-ICP-MS system used in silicate and oxide mineral analyses. LA-ICP-MS analysis was performed using a laser pulse rate of 5 Hz and spot size of 37–50 μm. The contents of Ru, Rh, and Pd could not be measured due to high molecular interferences of Ni- and Cu-argide generated from ablation of the sulfide. An analysis consisted of 30 s of background measurement followed by 40 s of sample ablation. CANMET po727 FeS standard described in Barnes et al. (2008) and Park et al. (2012a) was used as the external standard with the Fe concentration obtained from EPMA employed as the internal standard. The

MASS-3 (USGS) sulfide reference material containing ~30–100 ppm of PGE and Au was used to monitor quality control. The result of triplicate analyses of the MASS-3 agrees with values from Fonseca (2007). Data reduction was performed following the method used for silicate and oxide minerals.

Whole rock trace element analysis

Trace elements in nine whole rock samples were analyzed by LA-ICP-MS following the method described in Campbell (2003) and using the same LA-ICP-MS system used to analyze silicate minerals. Glass discs were made using 0.5 g of sample powder and 1.5 g of lithium borate eutectic flux (12:22 $Li_2B_4O_7$: $LiBO_2$ mass ratio). Analyses were obtained at a laser repetition rate of 5 Hz with a spot size of 105 μm. Each spot analysis consisted of 30 s of background measurement followed by 40 s of sample ablation. The NIST 612 standard was analyzed before and after analyses of 6 points on each sample. The BCR-2 g (USGS) was used to monitor quality control. Ca concentrations measured by XRF from Wyborn (1983) and Ickert et al. (2011) were used as an internal standard to determine the absolute concentrations of the elements. Analytical uncertainties obtained by multiple analyses of BCR-2 g (USGS) were ±1 to 6 % (1σ), depending on the elements (Electronic supplementary materials). Analytical accuracy is better than 10 % for all elements as demonstrated in Electronic supplementary materials, where our measured values for BCR-2 g are compared with the reference values from Gao et al. (2002) and GeoReM database (http://georem.mpch-mainz.gwdg.de/).

Whole rock PGE and Re analysis

Twelve samples were selected covering all rock types from the gabbro to the aplite for PGE and Re analysis. The selected rocks were powdered in an alumina mill. Whole rock PGE (Pd, Pt, Rh, and Ir) and Re concentrations in the BPZP were measured using a Ni-sulfide fire assay-isotope dilution method described by Park et al. (2012b). Briefly, 2–5 g of sample powder was mixed with Ni, S, and sodium borax powder (S252-10, Fisher Scientific) in the ratio of sample: Ni:S:Na-borax = 10:1:0.5:10. These components were mixed thoroughly and transferred into a porcelain Coors™ crucible. A mixed spike solution of PGE (^{105}Pd, ^{185}Re, ^{191}Ir, and ^{195}Pt) was added to the mixture and fused in a preheated furnace at 1,100 °C for 30 min. After quenching, the Ni-sulfide beads were collected and dissolved in HCl. The solution was filtered through a filter paper prior to digestion of the filter paper in aqua regia. The solution was then dried down to approximately ~100 μl, and diluted with 2 % HNO_3 prior to its analysis by ICP-MS.

An Agilent 7500 quadrupole ICP-MS at the ANU was used to measure the isotopes of Re and PGE. All samples were analyzed in duplicate or triplicate to assess heterogeneity of a sample powder aliquant except for BP12. The sensitivities in each analysis using the Agilent 7500 ICP-MS were 2.6–5.5 × 10^4 cps/ppb for mass 89, 2.9–4.5 × 10^4 cps/ppb for mass 140 and 2.4–2.9 × 10^4 cps/ppb for mass 205. Some of the duplicate (second) samples were reanalyzed by a single collector Agilent 7700× ICP-MS, which provided higher sensitivity of 1.5–2.3 × 10^5 cps/ppb for masses 89, 140, and 205 than the Agilent 7500 ICP-MS. The data obtained using both ICP-MS are compared in Electronic supplementary materials and they agree well each other within 1σ uncertainty. The data obtained using an Agilent 7700× ICP-MS were finally taken for interpretation.

Potential molecular interferences on the analyzed isotopes were monitored by measuring solutions containing Ni, Cu, Zn, Co, Hf, Mo, Zr, and Ta. The effects of the molecular interference were subtracted using measured oxide and argide production rates. The correction rate is <0.5 % for all PGE. Concentrations of Pd, Pt, Rh, Ir, and Re were determined by isotope dilution. Concentrations of monoisotopic Rh were corrected by a method similar to that of Meisel et al. (2003), which uses count rates of ^{103}Rh and ^{106}Pd, making the assumption that any loss of Rh during the analytical procedure was similar to the loss of Pd. The detail of calculation is described by Park et al. (2012b).

Procedural blanks were determined from sample-free analyses using 5 g of sodium borax, 0.5 g of Ni, and 0.25 g of S for every session. Average procedural blanks based on five separate fusion blanks were 0.5 ± 0.3 ppt for Ir, 0.8 ± 0.6 ppt for Rh, 8 ± 7 ppt for Pt, 10 ± 3 ppt for Pd, and 10 ± 2 ppt for Re (1σ). The method detection limits (MDL), taken to be three standard deviations of the procedural blanks, were 0.9 ppt for Ir, 1.8 ppt for Rh, 20 ppt for Pt, 9 ppt for Pd, and 7 ppt for Re.

Results

Ni, Cu, and Re concentrations in silicate and oxide minerals

Nickel, Cu, and Re concentrations in the major silicate and oxide minerals of the BPZP were measured by LA-ICP-MS analyses to evaluate the importance of these minerals as hosts for Ni, Cu, and Re. The results are presented in Table 1. Where possible, cores of unaltered grains of all silicate and oxide minerals were selected for analyses. The analyzed hornblendes and biotites are either interstitial phases to phenocrysts or reaction rims on the

Table 1 Summary of Ni, Cu, and Re concentrations in silicate and oxide minerals by LA-ICP-MS, silicate, and oxide mineral control on whole rock Ni, Cu, and Re, and fraction of chalcopyrite in the BPZP

Sample	Rock type	Plagioclase		Hornblende			Biotite			Clinopyroxene			Orthopyroxene			Magnetite				Ilmenite				$Ni_{sil+oxi}/Ni_{WR}$ (%)[a]	$Cu_{sil+oxi}/Cu_{WR}$ (%)[a]	$Re_{sil+oxi}/Re_{WR}$ (%)[a]	Chalcopyrite (wt %)[b]
		n	Cu	*n*	Ni	Cu	*n*	Ni	Cu	*n*	Ni	Cu	*n*	Ni	Cu	*n*	Ni	Cu	Re	*n*	Ni	Cu	Re				
BP4	Type-1 Gabbro	15	2.3	4	63	3.4	4	148	2.3	#	129	14		119	0.07	–	–	–	–	–	–	–	–	82	2.9	–	0.039
BP2	Type-1 Gabbro	6	0.2	10	83	3.4	7	158	7.2	5	106	0.2		131	0.05	3	105[c]	0.5[c]	b.d.l.[c]	2	19[c]	6.6[c]	b.d.l.[c]	122	1.2	–	0.025
BP3	Type-2 Gabbro	15	0.7	2	66	1.4	4	151	0.6	5	126	0.2		113	0.04	3	142	0.4	6.9	1	35	5.4	3.9	108	0.7	63	0.025
BP39	Type-2 Gabbro	12	1.1	3	94	4.5	6	176	29	8	77	1.3		79	0.03	3	182	0.3	16	5	30	6.7	11	100	3.8	79	0.019
BP40	Outer granodiorite	11	0.9	9	71	0.8	4	131	0.5	5	92	0.3	–	–	–	2	96	0.2	b.d.l.	–	–	–	–	98	1.3	–	0.019
BP24	Outer granodiorite	11	1.0	7	67	2.9	4	120	4.9	5	89	26	–	–	–	–	–	–	–	–	–	–	–	94	8.9	–	0.011
BP14	Inner granodiorite	6	0.2	7	26	4.6	2	45	1.8	–	–	–	–	–	–	–	–	–	–	–	–	–	–	81	3.4	–	0.012
BP30	Granite	15	0.3	5	72	5.6	2	127	3.7	–	–	–	–	–	–	–	–	–	–	–	–	–	–	70	7.3	–	0.009
BP21	Granite	6	0.3	4	65	5.7	3	130	5.7	–	–	–	–	–	–	–	–	–	–	–	–	–	–	73	13	–	0.003
BP19	Granite	11	0.2	1	–	2.0	3	–	6.2	–	–	–	–	–	–	–	–	–	–	–	–	–	–	92	2.3	–	0.015

Ni and Cu concentrations are in ppm and Re concentrations are in ppb. *n* represents number of analyses

[a] Calculated using whole rock Ni and Cu contents from Table 5 and modal analysis results from Wyborn (1983); $Metal_{sil+oxi}$ = Metal contents in silicate and oxide minerals; $Metal_{WR}$ = Metal contents in whole rock

[b] Cu contents in chalcopyrite was assumed to be 34.6 wt %

[c] Ni, Cu, and Re contents in BP1 (Type-1 gabbro)

clinopyroxene in the gabbros and the granodiorites, whereas they are euhedral to subhedral crystals in the granites.

There is no clear correlation between Ni and Cu concentrations in silicate and oxide minerals, whole rock Ni and Cu contents, or rock type. The average Cu concentrations in silicate and oxide minerals are mostly less than 8 ppm although some biotite and clinopyroxene from the gabbro and the inner granodiorite contain average Cu concentrations of up to 29 ppm (Table 1). Nickel is much more compatible than Cu in the silicate and oxide minerals and typical Ni concentrations are 45–176 ppm in biotite, 65–94 ppm in hornblende, 77–129 ppm in clinopyroxene, 79–131 ppm in orthopyroxene, 96–182 ppm in magnetite, and 19–35 ppm in ilmenite (Table 1). Nickel and Cu contents in orthoclase and quartz were measured in selected samples. Average Cu concentrations are 0.9 ppm ($n = 4$) and 1.2 ppm ($n = 2$) in orthoclase and quartz, respectively, and Ni contents are below the detection limit of LA-ICP-MS (0.5 ppb) in both minerals.

Rhenium concentrations in magnetite and ilmenite from four samples of the gabbro and outer granodiorite were also measured by LA-ICP-MS (Table 1). The average Re contents vary from below the detection limit of 1.5 ppb to 16 ppb in these minerals. Re is enriched in magnetite and ilmenite from the whole rock samples that have the highest Re contents (BP3 and BP39).

Texture and composition of sulfides

Magmatic sulfide blebs are abundant in the gabbro and the granodiorite, but are rarely observed in the granite or the aplite. The relative abundance of the sulfide blebs is generally gabbro > outer granodiorite > inner granodiorite although the abundance in the gabbro is highly variable, for example, BP39 and BP3 contain fewer sulfide blebs than the BP40 and BP24 from the outer granodiorite.

The sulfide blebs have spherical or ovoid shapes and occur at the boundaries between cumulus pyroxene grains and neighboring interstitial phases (Fig. 3a–c) or within interstitial minerals such as hornblende, biotite, and quartz (Fig. 3d–i). Some of these sulfide blebs are associated with magnetite (Fig. 3i). The size of the blebs varies according to their occurrences. The sulfide blebs trapped in the margin of the pyroxene phenocrysts are mostly 1–10 μm in size (Fig. 3a, b), whereas those trapped in the interstitial minerals are larger in size (20–100 μm) and make up a high fraction of total sulfides (Fig. 3d–i).

The sulfide blebs consist of pyrrhotite, pyrite, chalcopyrite, and S-bearing Fe-oxide. This mineral assemblage is typical of magmatic sulfide blebs found in many other igneous rocks (Keith et al. 1997; Larocque et al. 2000; Stavast et al. 2006; Barnes et al. 2006, 2008). As a sulfide bleb cools, it firstly crystallizes monosulfide solid solution (MSS) leaving behind a Cu-rich fractionated sulfide melt. The Cu-rich melt crystallizes as intermediate solid solution (ISS) with further cooling (Ebel and Naldrett 1997; Barnes et al. 2006). Finally, pyrrhotite and pyrite are exsolved from the MSS and chalcopyrite from the ISS (Ebel and Naldrett 1997; Barnes et al. 2006). The S-bearing Fe-oxide can be a product of oxidation of the sulfides at low temperature, a result of chemical exchange between the sulfide and an adjacent silicate mineral (Larocque et al. 2000; Stavast et al. 2006) or a quenched product of dissolved oxygen components in sulfide melt (e.g., Fonseca et al. 2009). In volcanic and intrusive rocks associated with Cu–Au mineralization the sulfide are often severely oxidized and forms a spongy textured Fe-oxide by degassing and interaction with magmatic fluid (Keith et al. 1997; Larocque et al. 2000; Stavast et al. 2006). The Fe-oxides in the sulfide blebs from the BPZP do not show the spongy texture, indicating that the sulfide blebs did not experience such degassing. The mineral assemblage of the sulfide blebs varies greatly from an Fe-rich type, which consists dominantly of pyrrhotite and/or pyrite with minor chalcopyrite at the margins, (Fig. 3b, d-f and h-i) to a Cu-rich type that is mainly composed of chalcopyrite with little Fe-sulfide (Fig. 3a, c, g).

The compositions of the sulfide and S-bearing Fe-oxide, obtained by the electron microprobe analyses, are shown in Tables 2 and 3, respectively. Pyrrhotite, pyrite, and chalcopyrite contain significant amount of trace metals such as Co, Ni, Cu, Ag, and Pb and the cumulative weight percent of these metals can be up to 16 wt % in some analyses (Table 2). The composition of the sulfides is consistent with that of magmatic sulfides as reported in previous studies (Larocque et al. 2000; Stavast et al. 2006). Also shown in Table 2 is the composition of secondary sulfides, which are often disseminated in sericitized plagioclase or filling the cracks of altered silicate minerals. The composition of sulfides from the sulfide blebs is distinguished from the secondary sulfides by the low Co, Ni, Ag, and Pb contents of the latter, all of which are below the limit of detection (Table 2). The analytical total for a pyrrhotite (BP1-5) is low. Larocque et al. (2000) also report low totals for magmatic sulfides. They attributed the low total to oxide components in magmatic sulfides, which could not separate from sulfide due to quenching. It was shown by experimental studies on oxygen contents in immiscible sulfide liquid (Fonseca 2007; Fonseca et al. 2009) that magmatic sulfide can contain up to 30 wt % oxygen and that the oxygen content increases with increasing fO_2 and decreasing fS_2. The S-bearing Fe-oxide from sulfide blebs contains 0.37–0.57 wt % SO_3 with various amount of MgO, SiO_2, NiO, and CuO (Table 3), which are clearly distinguished from typical compositions of Ti–Fe oxide

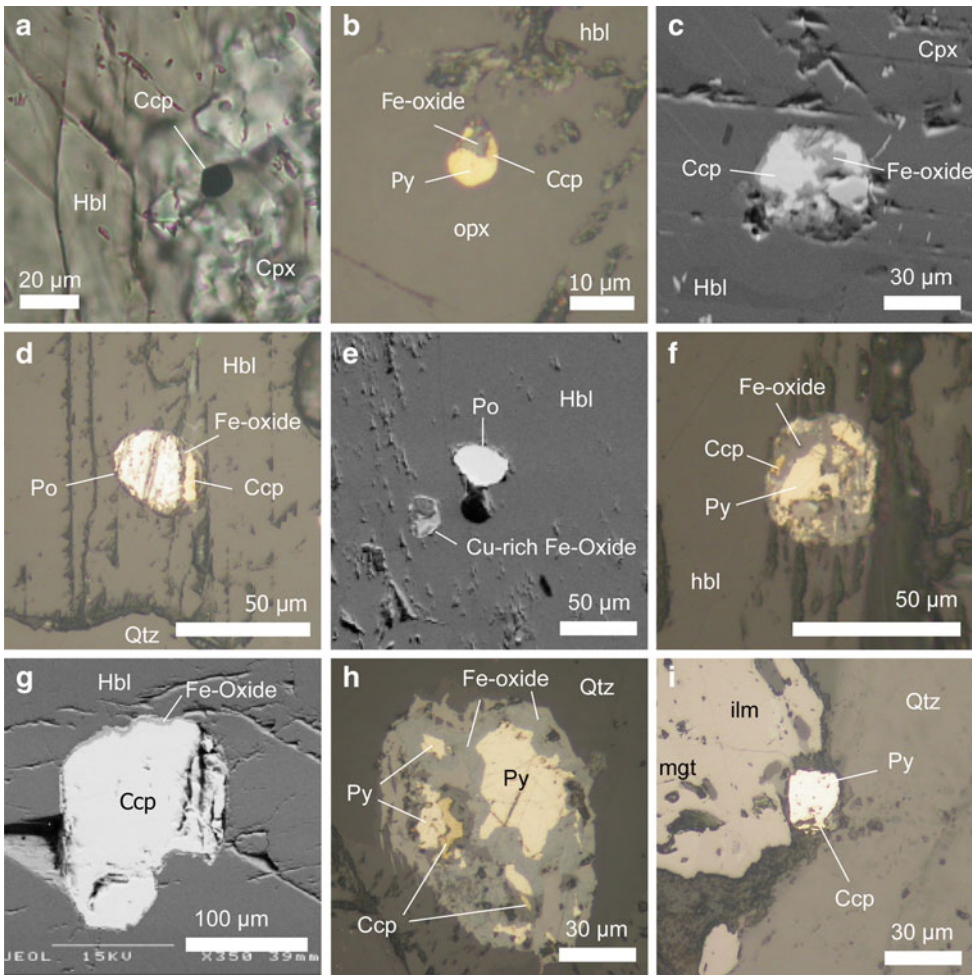

Fig. 3 Optical microscope and BSE images of sulfide blebs from the BPZP. **a** Round Ni-bearing chalcopyrite at the boundary between a cumulus clinopyroxene and its reaction rim of hornblende from the outer granodiorites (BP24). **b** Ovoid sulfide bleb that occurs at the boundary between a cumulus orthopyroxene and interstitial hornblende from a Type-1 gabbro (BP1). The sulfide bleb mainly consists of pyrite with minor chalcopyrite and S-bearing Fe-oxide. **c** Round chalcopyrite-rich sulfide bleb trapped at the margin of a cumulus clinopyroxene from a Type-2 gabbro (BP3). **d** Ovoid pyrrhotite-rich sulfide bleb trapped in interstitial hornblende from a Type-1 gabbro (BP1). The pyrrhotite contains trace metals (Co, Ni, Cu, Ag, and Pd) of 1.3 wt %. **e** Round Ni-bearing pyrrhotite that occurs in an interstitial hornblende from the outer granodiorite (BP7). Note that the *gray skeletal grain* is a Cu-rich Fe-Oxide, which may have separated from Fe-rich sulfide that formed adjacent pyrrhotite. **f** Round sulfide bleb trapped in an interstitial hornblende from a Type-1 gabbro (BP1) that is composed of pyrite and S-bearing Fe-oxide with minor chalcopyrite. **g** Cu-rich sulfide bleb trapped in an interstitial hornblende rimed by S-bearing Fe- oxide from a Type-1 gabbro (BP1). LA-ICP-MS time-resolved spectrum shows that the chalcopyrite is aggregated with pentlandite, Pt and Au alloys (Fig. 4a). **h** Ovoid sulfide bleb trapped in an interstitial quartz crystal from a Type-1 gabbro (BP1). The pyrite grain contains 0.03–0.07 wt % and 0.55 wt % Ni and Cu, respectively. LA-ICP-MS time-resolved spectrum shows that this pyrite is aggregated with Re-sulfide (Fig. 4c), **i** A sulfide bleb that occurs in an interstitial quartz crystal associated with ilmenite and magnetite from the outer granodiorite (BP40). *Ccp* chalcopyrite, *Cpx* clinopyroxene, *Hbl* hornblende, *Ilm* Ilmenite, *Mgt* magnetite, *Opx* orthopyroxene, *Po* pyrrhotite, *Py* pyrite

from the BPZP, such as magnetite and ilmenite (Table 3). Analytical totals for the S-bearing Fe-oxide are low with a range from 74 to 80 wt %. This is probably because Fe^{3+}/Fe^{2+} ratios are higher in the S-bearing Fe-oxide than magnetite because FeO and Fe_2O_3 contents in the S-bearing Fe-oxide were calculated according to charge balance and stoichiometry of the magnetite-ulvöspinel solid solution. However, if we assume all Fe is present as Fe_2O_3 in the Fe-oxide, it is still not sufficiently high to explain the low totals. The cause of the low analytical totals for Fe-oxide is not clear but this phenomenon was also observed by Larocque et al. (2000) who attributed it to the presence of void space partially filled with glass that was not observed in this study.

The LA-ICP-MS analyses of sulfide blebs provide three-dimensional information on the composition of the sulfide bleb (Fig. 4; Table 4). Figure 4a shows the spectra of a chalcopyrite from a Cu-rich sulfide bleb (BP1-7-27 in Table 2; Fig. 3g). The ablation signal can be divided into two parts; the first corresponds to chalcopyrite and the

Table 2 Results of electron microprobe analyses of sulfides (wt %)

Analysis No.	Mineral	S	Fe	Co	Ni	Cu	Ag	Pb	Total
Sulfides from sulfide blebs									
BP1-1[a]	Po	36.8	59.3	<0.17	0.21	8.66	<0.02	<0.07	105.0
BP1-2[a]	Po	36.0	54.7	<0.17	0.10	16.0	<0.02	<0.07	106.8
BP1-5[a]	Po	39.7	48.2	0.19	0.90	0.12	0.02	0.10	89.2
BP7-3-3 s	Po	38.6	60.0	<0.19	0.33	<0.19			98.9
BP1-3[a]	Py	53.5	47.0	<0.17	0.03	<0.1	<0.02	<0.07	100.5
BP1-4[a]	Py	53.6	46.5	<0.17	0.07	0.55	<0.02	<0.07	100.7
BP40-7-2	Py	53.3	46.8	<0.19	<0.14	0.22			100.4
BP7-9-1 s	Py	53.7	43.6	4.45	0.40	<0.19			102.2
P40-6-5	Py	52.5	45.6	<0.19	1.03	0.58			99.7
BP24-6-1 s	Ccp	31.9	24.4	<0.19	<0.14	43.1			99.4
BP24-6-2 s	Ccp	34.1	30.2	<0.19	0.22	33.5			98.1
BP1-7-27	Ccp	34.1	30.2	<0.19	<0.14	34.7			99.1
BP3-9-2	Ccp	34.1	31.0	<0.19	<0.14	34.2			99.5
BP3-12-1	Ccp	34.6	30.9	<0.19	<0.14	34.5			99.9
BP24-4-2 s	Ccp	34.8	29.7	<0.19	<0.14	34.5			99.0
BP7-7-6 s	Ccp	34.5	30.4	<0.19	<0.14	33.5			98.5
Secondary sulfide									
BP1-S1[a]	Ccp	35.1	31.2	<0.17	<0.03	33.2	<0.02	<0.07	99.5
BP1-S7[a]	Ccp	34.9	30.8	<0.17	<0.03	32.7	<0.02	0.10	98.5
BP24-7-1 s	Ccp	34.4	30.1	<0.19	<0.14	34.8			99.3
BP7-6-1 s	Ccp	34.5	30.1	<0.19	<0.14	34.1			98.7
BP7-8-1 s	Ccp	34.5	30.9	<0.19	<0.14	34.6			100.0
BP3-6-1	Ccp	34.3	30.9	<0.19	<0.14	34.2			99.4
BP40-4-1	Ccp	34.1	30.5	<0.19	<0.14	33.8			98.4

Po pyrrhotite, *Py* pyrite, *Ccp* chalcopyrite

[a] Data measured by EX100 electron microprobe in WDS. Other data were measured by JEOL6400 SEM in EDS mode

second to a mixture of host chalcopyrite and Ni, Pt, and Au-rich inclusions. The chalcopyrite contains ~90 ppb Pt and the inclusion-chalcopyrite mixture contains 290 ppb of Pt and 300 ppb of Au, with Ir and Os that are below the detection limit in both phases (Table 4). The Ni, Pt, and Au-rich inclusions are probably pentlandite and/or Pt and Au alloys that have crystallized from the Cu-rich sulfide melt during cooling. The presence of platinum group minerals is frequently observed in the time-resolved spectra of a sulfide bleb entrapped in magnetite as peaks of Pt and Ir in the signal (Fig. 4b). The concomitant occurrence of Pt and Ir peaks and absence of a Pd peak suggest that the inclusions are unlikely to be Pt–Pd rich sulfosalt minerals (e.g., Tomkins 2010). Figure 4c shows the spectra of a pyrite from an Fe-rich sulfide bleb (BP1-4 in Table 2; Fig. 3h), and a peak of Re in the signal corresponds to a Re-rich inclusion trapped in the pyrite. The pyrite contains ~240 ppb Pt and ~50 ppb Au, with Ir and Os that are below the detection limit. Platinum, Au, and Re are commonly present in such discrete mineral inclusions (e.g., Pt- or Au-rich alloys and Re-rich sulfides) in magmatic sulfide blebs from PGE-rich reefs from various layered intrusions and subvolcanic sills (Barnes et al. 2006; 2008; Dare et al. 2010, 2011).

Ni, Cu, Re, and PGE concentrations of whole rock samples

The whole rock trace element concentrations and Re and PGE concentrations are given in Tables 5 and 6, respectively. All the PGE and Re data reported in Table 6 have had an average blank subtracted. The uncertainty in the PGE and Re data comes mainly from the blank subtraction and the ICP-MS counting statistics, which is presented as 1σ in Table 6. Average Re and PGE concentrations are used in Figs. 5, 6, and 7 except for some heterogeneous samples for which replicate analyses are provided if RSD (1σ) > 50 %. For these samples, one or two analyses of individual sample aliquot is/are presented in order to investigate the nugget effect. Accuracy and precision of the analyses were tested by replicate analyses of the reference material TDB-1 (CANMET diabase) (Table 7). The TDB-1

Table 3 Results of electron microprobe analyses of S-bearing Fe-oxides and Ti–Fe oxide phenocrysts (wt %)

Analysis No.	MgO	Al_2O_3	SiO_2	FeO[a]	$Fe_2O_3^a$	Cr_2O_3	MnO	V_2O_3	NiO	TiO_2	CuO	SO_3	Total
S-bearing Fe-oxide from sulfide blebs													
BP40-2-3	0.50	<0.06	10.9	26.4	24.9	<0.09	<0.09	<0.07	<0.18	<0.08	11.08	0.37	74.2
BP40-7-3	0.46	<0.06	2.65	27.0	48.8	<0.09	<0.09	<0.07	0.27	<0.08	0.49	0.45	80.2
BP1-7-2 s	0.61	<0.06	10.4	23.4	27.6	<0.09	<0.09	<0.07	<0.18	<0.08	14.04	0.57	76.6
Magnetite													
BP1-1-1	0.07	0.24	0.10	30.9	65.5	0.24	<0.09	1.37	<0.18	0.21	<0.25	<0.07	98.6
BP1-1-8	0.04	0.43	0.04	31.2	65.9	0.12	0.10	1.53	<0.18	0.29	<0.25	<0.07	99.7
BP40-5-1	0.05	0.31	0.15	31.6	64.3	0.55	<0.09	0.98	<0.18	0.82	<0.25	<0.07	98.8
BP40-7-4	0.50	2.41	0.13	32.9	57.4	2.58	0.14	1.42	<0.18	2.33	<0.25	<0.07	99.8
BP40-10-1	0.06	0.86	0.09	34.0	57.3	1.56	0.20	0.92	<0.18	3.63	<0.25	<0.07	98.6
BP40-11-1	0.12	0.45	0.07	30.8	65.8	0.48	0.04	1.00	<0.18	0.14	<0.25	<0.07	99.0
Ilmenite													
BP1-6-26	0.16	0.11	<0.03	41.5	6.0	<0.09	2.83	<0.07	<0.18	49.7	<0.25	<0.07	100.3
BP1-9-29	0.09	<0.06	<0.03	40.7	6.4	<0.09	3.59	<0.07	<0.18	49.5	<0.25	<0.07	100.3
BP1-8-30	0.13	<0.06	<0.03	41.8	5.8	<0.09	2.62	<0.07	<0.18	49.7	<0.25	<0.07	100.0
BP40-4-2	0.04	<0.06	<0.03	40.0	5.2	<0.09	4.75	<0.07	<0.18	49.9	<0.25	<0.07	99.9
BP40-6-1	0.08	<0.06	<0.03	40.4	7.6	<0.09	3.30	<0.07	<0.18	48.8	<0.25	<0.07	100.1

All data measured by JEOL6400 SEM in EDS mode

[a] FeO and Fe_2O_3 of magnetite and ilmenite were calculated by stoichiometry and charge balance (Carmichael 1966)

Table 4 Ir, Os, Pt, and Au concentrations in chalcopyrite from sulfide bleb (ppm)

Analysis No.	Os	Ir	Pt	Au
BP1-7-27 (Segment 1)	<0.07	<0.02	0.09	<0.02
BP1-7-27 (Segment 2)	<0.12	<0.04	0.29	0.30
BP1-4	<0.003	<0.001	0.24	0.05
MASS3 reference material				
#1	103	72	31	71
#2	106	75	33	77
#3	98	70	34	79
Fonseca (2007)[a]	96	67	33	73

[a] Analyzed by acid digestion and ICP-MS

analyses gave reproducibility of RSD (1σ) < 11 % for Rh, Pt, and Pd except for Ir (19 %) and Re (21 %) and averages agree with the certified values (Govindaraju 1994) and the values reported by Meisel and Moser (2004) and Peucker-Ehrenbrink et al. (2003) within error (2σ).

Gabbro

Nickel, Cu, Re, and PGE concentrations in the gabbro do not show any clear trend when plotted against MgO although the compositional variation is only 1.1 wt % MgO (Fig. 5). MgO had been used as a fractionation factor in order to distinguish relatively mafic outer granodiorite from felsic inner granodiorite, which contain similar SiO_2 (e.g., Wyborn et al. 2001). On a primitive mantle-normalized diagram (Fig. 6a), two types of the gabbro are recognized; Type-1 gabbro contains high Pd and Pt concentrations with high Pd/Ir ratio (Pd = 5.8–7.9 ppb; Pt = 4.0–4.9 ppb; Pd/Ir = 81–224) and Type-2 gabbro contains low Pd and Pt concentrations with low Pd/Ir ratio (Pd = 2.7–3.8 ppb; Pt = 2.8–4.6 ppb; Pd/Ir = 30–110).

Granodiorite

Nickel, Cu, Re, and PGE concentrations decrease as MgO contents decrease in the granodiorite (Fig. 5). The outer granodiorite contain 2.9–5.0 ppb of Pd, 2.0–2.8 ppb of Pt, and 0.17–0.18 ppb of Re that are similar to the concentrations in the gabbro (Figs. 5d, e, 6a; Table 7). In contrast Ni, Rh, and Ir concentrations are lower in the outer granodiorite by a factor of 2–5 times compared with the gabbro. The similarity in Pd and Pt concentrations between the granodiorite and the gabbro is significant because the difference in MgO contents between the gabbro and the outer granodiorite is 2–3 wt %. Patterns for chalcophile elements and PGE for the granodiorites are sub-parallel to

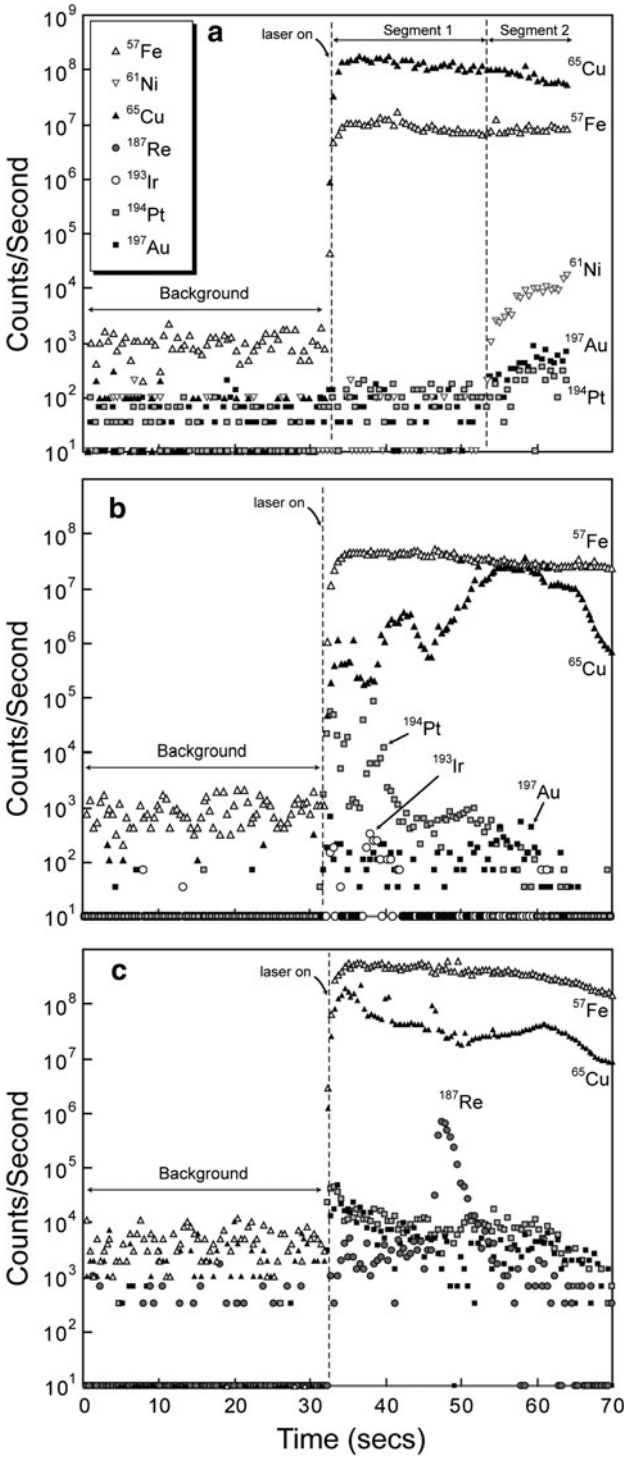

Fig. 4 Time-resolved LA-ICP-MS spectra for sulfide blebs. **a** A chalcopyrite grain in a Cu-rich sulfide bleb from a Type-1 gabbro (BP1). The spectrum can be divided into two segments with different Ni, Au, and Pt contents. **b** An Fe-rich sulfide bleb trapped in magnetite from outer granodiorite (BP40). The peaks of Pt, Ir, and Au represent the presence of Pt, Ir, and Au bearing inclusions. **c** A pyrite grain in an Fe-rich sulfide bleb from a Type-1 gabbro (BP1). The Re peak corresponds a Re-sulfide inclusion

each other on a mantle-normalized diagram, with high Pd/Ir ratio ranging from 324 to 381, except for BP7-II (Figs. 6b, 7b; Table 7).

Granite and aplite

Nickel, Cu, Re, and PGE concentrations show clear negative correlations with MgO contents in the granite and the aplite (Fig. 5). It should be noted, however, that there is a clear discontinuity between the granite and the granodiorite in the trends for Ni, Rh, and Ir against MgO (Fig. 5b, g, h). Iridium concentrations in the granite are even higher than for most of the granodiorite samples (Fig. 5h). Chalcophile elements patterns for the granite and aplite are sub-parallel to each other on a mantle-normalized diagram, with low Pd/Ir ratio ranging from 29 to 53, except for BP19-I (Fig. 6c; Table 7).

Discussion

Control of silicate and oxide minerals on the whole rock Cu, Ni, and Re variations

Copper and Ni show positive correlations with MgO across all rock types, indicating compatible behavior of these elements during magma/magma batch evolution (Fig. 5f, g). Mass balance calculations were carried out to investigate the role of silicate and oxide minerals in the whole rock Cu and Ni budgets and to constrain the abundance of sulfide in the BPZP. The calculations were performed using the average Cu and Ni contents of the silicate and oxide minerals (Table 1), whole rock Cu and Ni contents (Table 6) and the modal fraction of each mineral (Wyborn 1983). Copper and Ni contents of the minerals are assumed to be the same as those from other minerals analyzed in the same rock type in cases where the data were not obtained directly. The detection limit (0.5 ppb) was assumed as the concentration for Ni contents in quartz and orthoclase.

The results show that the amount of Cu held in silicate and oxide minerals is 0.7–13 wt % of the whole rock Cu budget (Table 1). Therefore, the Cu that cannot be accounted for in the budget is attributed to Cu held in the sulfide blebs. Although we did not consider accessory minerals, such as apatite and titanite for the mass balance calculation, the fraction of Cu hosted by these minerals will be negligible because of their low modal abundance (0.4–0.7 modal %; Wyborn 1983) and weak affinity for Cu (Paster et al. 1974). If it is entirely held in chalcopyrite, the weight fractions of chalcopyrite in the BPZP can be calculated as being between 0.003 and 0.039 wt % (Table 1). The weight fraction of chalcopyrite declines from the

Table 5 Trace element concentrations in the BPZP measured by LA-ICP-MS (ppm)

Rock type	Type-1 Gabbro	Type-2 Gabbro	Outer granodiorite		Inner granodiorite		Granite		Aplite
Sample No.	BP5	BP39	BP7	BP24	BP14	BP16	BP18	BP19	BP12
Sc	35.3	34.0	26.0	25.6	25.0	23.5	14.0	12.0	6.3
Cr	244	172	156	140	55.9	107	89.9	74.0	16.5
Co	29.3	42.8	31.8	19.0	28.9	37.2	34.4	29.5	30.8
Mn	1,078	1,072	811	781	924	823	508	488	239
Ni	52.4	43.7	40.3	29.4	14.0	22.1	24.2	19.3	6.7
Cu	81.1	69.7	95.8	41.4	44.1	36.8	36.7	13.6	2.8
Zn	53.6	52.9	48.3	45.9	62.3	50.4	29.6	25.7	11.3
Ga	13.7	13.8	13.7	13.5	15.5	14.9	13.8	13.4	12.9
Rb	41	35	78	71	67	73	114	141	183
Sr	595	532	606	633	742	620	405	327	182
Y	17.6	17.1	18.6	18.2	19.0	19.3	21.0	21.1	27.9
Zr	73	83	124	115	130	128	154	149	157
Nb	3.6	3.2	7.0	6.7	6.3	7.3	9.4	9.8	10.9
Mo	0.91	1.04	1.37	1.21	1.26	1.01	1.69	0.72	1.03
Sn	3.34	2.19	2.52	2.25	2.25	2.36	2.81	2.91	3.40
Cs	3.28	1.41	3.33	2.95	2.60	2.93	3.78	4.97	6.10
Ba	338	365	698	651	690	591	918	800	740
La	18.3	13.9	29.2	35.6	36.0	35.0	43.9	64.7	53.9
Ce	35.5	28.1	56.2	59.8	66.8	67.3	79.1	87.3	78.4
Pr	4.34	3.52	6.55	7.18	7.79	7.70	8.57	10.7	10.8
Nd	18.2	15.1	25.8	28.2	31.4	30.2	31.3	35.9	37.9
Sm	3.92	3.42	5.10	5.31	6.07	5.65	5.72	5.56	6.76
Eu	1.13	0.97	1.21	1.31	1.65	1.36	1.22	1.04	0.90
Gd	3.71	3.47	4.36	4.47	5.08	4.65	4.62	4.43	5.87
Tb	0.55	0.51	0.59	0.59	0.64	0.62	0.65	0.62	0.81
Dy	3.44	3.22	3.62	3.53	3.82	3.69	3.94	3.64	4.85
Ho	0.69	0.66	0.69	0.68	0.72	0.71	0.77	0.75	0.96
Er	2.02	1.94	2.03	1.94	2.10	2.08	2.30	2.27	2.77
Tm	0.29	0.27	0.29	0.28	0.29	0.30	0.32	0.33	0.38
Yb	1.82	1.77	1.92	1.83	1.90	1.98	2.13	2.27	2.59
Lu	0.28	0.26	0.28	0.27	0.28	0.30	0.31	0.34	0.39
Hf	2.23	2.27	3.31	3.13	3.41	3.48	4.21	4.36	4.74
Ta	0.32	0.63	0.96	0.54	0.90	1.21	1.57	1.64	2.25
Pb	6.0	5.5	11.0	10.5	9.1	10.2	10.3	10.6	16.8
Th	5.2	4.1	9.9	9.6	10.0	11.0	16.3	21.0	31.7
U	1.14	0.91	2.14	2.32	2.61	2.60	3.30	4.22	7.76

gabbro to the granite. Note that the Type-1 gabbro contains more abundant sulfide (0.025–0.039 wt %) than the Type-2 gabbro (0.019–0.025 wt %) (Table 1). This is consistent with the observed relative abundance of magmatic sulfide in the BPZP rocks. The mass balance calculation and the presence of magmatic sulfide blebs in the BPZP clearly indicate that the whole rock Cu contents in the BPZP rocks are controlled by the segregation and distribution of the immiscible sulfide blebs during magma differentiation and that the influence of silicate and oxide minerals is negligible.

In contrast, the mass balance calculations show that most of the Ni is hosted by major silicate minerals (>70 wt %; Table 1), indicating that the compatible behavior of Ni in the BPZP resulted from fractional crystallization of mafic silicate minerals which have high Ni contents (Fig. 5b). This result is consistent with the lack of pentlandite in magmatic sulfide blebs from the BPZP. The

Table 6 PGE and Re concentrations in the BPZP (ppb)

Sample	n^a	Ir	σ^b	Rh	σ	Pt	σ	Pd	σ	Re	σ	Pd/Ir	Cu/Pd × 1000
Type-1 Gabbro													
BP1 average	3	0.040		0.181		4.86		7.87		0.048		196	6.1
BP1 (#1)		0.042	0.004	0.180	0.015	5.59	0.18	7.85	0.39	0.049	0.005		
BP1 (#2)		0.038	0.005	0.170	0.010	4.35	0.15	8.23	0.23	0.050	0.010		
BP1 (#3)		0.041	0.004	0.194	0.008	4.66	0.08	7.52	0.21	0.045	0.006		
BP5-I average[c]	2	0.026		0.138		4.04		5.77		0.093		224	14.0
BP5 (#1)		0.026	0.004	0.129	0.009	4.10	0.19	4.92	0.26	0.098	0.009		
BP5 (#2)		0.025	0.002	0.148	0.006	3.99	0.10	6.62	0.15	0.088	0.009		
BP5-II[c]	1	0.077	0.005	0.100	0.008	4.50	0.16	6.22	0.24	0.109	0.008	81	13.0
Type-2 Gabbro													
BP3-I[c]	1	0.037	0.006	0.186	0.012	3.33	0.09	3.80	0.10	0.136	0.045	101	23.2
BP3-II[c]	1	0.116	0.009	0.196	0.011	4.58	0.19	3.42	0.10	0.107	0.012	30	25.7
BP39 average	3	0.025		0.126		2.80		2.73		0.203		110	25.7
BP39 (#1)		0.021	0.002	0.132	0.004	3.09	0.08	2.52	0.10	0.267	0.063		
BP39 (#2)		0.034	0.007	0.107	0.006	2.80	0.09	2.71	0.07	0.218	0.011		
BP39 (#3)		0.020	0.004	0.138	0.009	2.51	0.06	2.96	0.13	0.123	0.010		
Outer granodiorite													
BP7-I average[c]	2	0.015		0.090		2.78		4.96		0.175		324	19.3
BP7 (#1)		0.017	0.004	0.089	0.006	2.94	0.13	5.17	0.11	0.169	0.017		
BP7 (#2)		0.014	0.005	0.090	0.005	2.63	0.04	4.76	0.21	0.177	0.020		
BP7-II[c]	1	0.045	0.004	0.093	0.006	2.81	0.08	4.73	0.16	0.177	0.020	105	20.3
BP24 average	2	0.008		0.074		1.96		2.88		0.172		358	14.3
BP24 (#1)		0.009	0.002	0.100	0.007	2.06	0.05	2.87	0.07	0.216	0.069		
BP24 (#2)		0.007	0.002	0.049	0.004	1.86	0.10	2.88	0.14	0.128	0.016		
Inner granodiorite													
BP14 average	3	0.004		0.016		0.52		1.42		0.092		381	31.0
BP14 (#1)		0.006	0.001	0.020	0.001	0.52	0.01	1.95	0.06	n.a.			
BP14 (#2)		0.003	0.001	0.012	0.001	0.52	0.01	1.16	0.05	0.096	0.004		
BP14 (#3)		0.003	0.001	0.016	0.001	0.51	0.03	1.15	0.05	0.089	0.005		
BP16 average	3	0.005		0.039		1.38		1.86		0.069		365	19.9
BP16 (#1)		0.005	0.001	0.041	0.003	1.65	0.09	1.85	0.06	0.076	0.009		
BP16 (#2)		0.005	0.001	0.040	0.002	1.26	0.02	1.65	0.03	0.079	0.012		
BP16 (#3)		0.005	0.0004	0.037	0.002	1.25	0.01	2.07	0.02	0.053	0.003		
Granite													
BP30 average	3	0.022		0.047		1.02		1.09		3.14		50	31.3
BP30 (#1)		0.025	0.004	0.054	0.002	0.92	0.04	1.21	0.04	n.a.			
BP30 (#2)		0.023	0.001	0.044	0.002	1.33	0.02	1.12	0.02	3.14	0.031		
BP30 (#3)		0.017	0.003	0.043	0.002	0.81	0.02	0.93	0.03	n.a.			
BP18 average	2	0.013		0.039		0.66		0.71		0.017		53	52.5
BP18 (#1)		0.013	0.0023	0.035	0.002	0.61	0.02	0.72	0.02	0.015	0.005		
BP18 (#2)		0.013	0.0030	0.044	0.004	0.71	0.03	0.69	0.03	0.019	0.005		
BP19-I[c]	1	0.072	0.010	0.085	0.007	0.63	0.03	0.68	0.03	0.012	0.007	9	20.7
BP19-II[c]	1	0.013	0.002	0.021	0.002	0.36	0.01	0.37	0.03	<0.007	0.003	29	38.1
Aplite													
BP12	1	0.001	0.0004	0.002	0.001	0.05	0.01	0.05	0.01	0.008	0.006	39	56.1

n.a. not analyzed

[a] *n* represents number of analyses

[b] Uncertainties are quoted at 1σ level

[c] Heterogeneous samples; each represents one or two analyses of individual sample aliquot

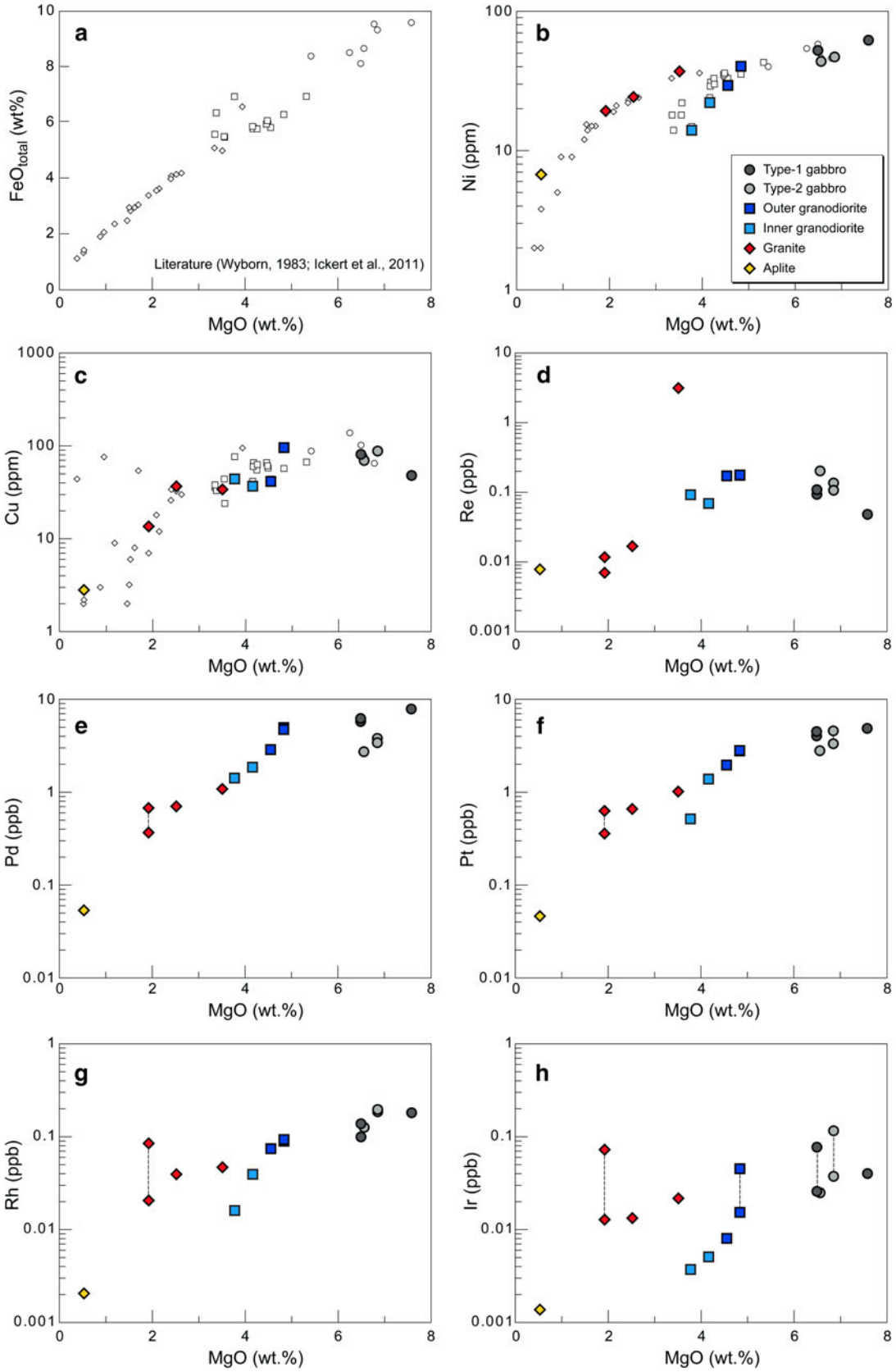

Fig. 5 Variation diagrams from FeO_{total}, Ni, Cu, Re, and PGE plotted against MgO for the BPZP. *Vertical lines* connect duplicate analyses that have large heterogeneity [> 50 % RSD (1σ)]. *Open symbols* are the data from Wyborn (1983) and Ickert et al. (2011)

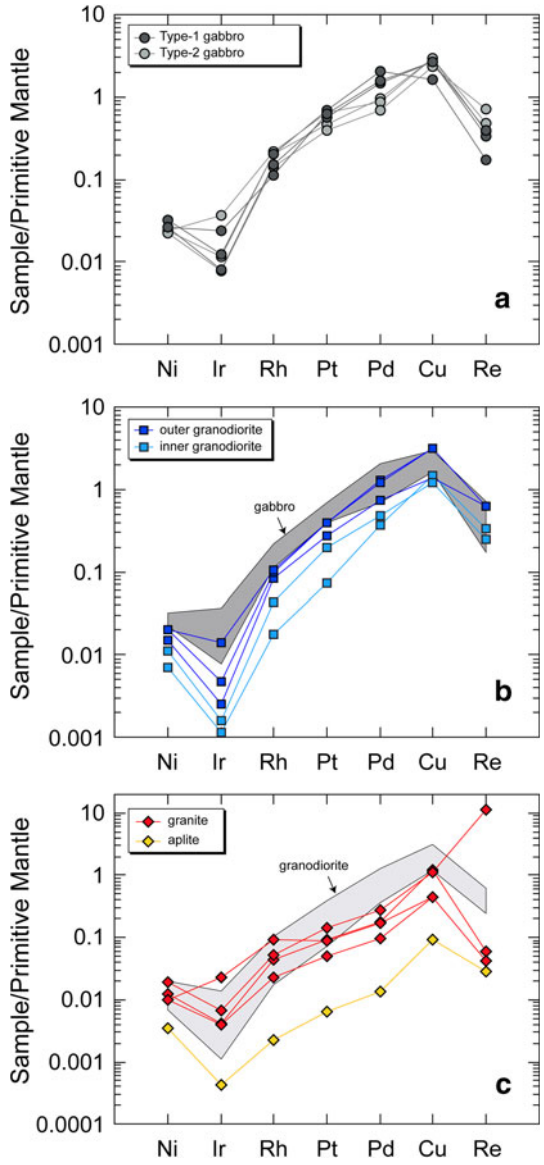

Fig. 6 Primitive mantle-normalized Ni, Cu, Re, and PGE concentrations in **a** gabbro, **b** granodiorite, and **c** granite and aplite. Normalizing values from McDonough and Sun (1995)

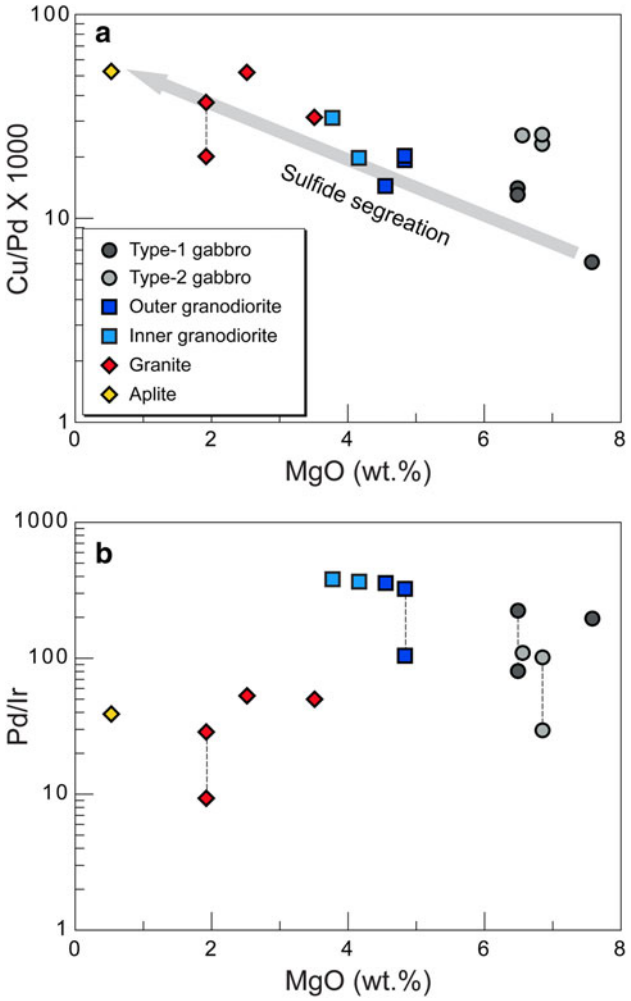

Fig. 7 Plots of **a** Cu/Pd and **b** Pd/Ir against MgO for the BPZP

estimates are slightly higher than 100 % in two samples (Table 1), which we attribute to the combined uncertainties arising from sampling, modal analyses, and LA-ICP-MS analyses.

The Re variation mimics that of Cu in Fig. 5 except for an anomalously high Re value in BP30. The high compatibility of Re with sulfide melts (Fonseca et al. 2007) and the presence of Re-rich inclusions in the sulfide blebs suggest that the immiscible sulfide phase (Fig. 4b, c) may be the principal host for Re in the same way that it hosts Cu. However, mass balance calculations performed using the average Re concentrations in magnetite and ilmenite (Table 1), whole rock Re contents (Table 6), and the modal fraction of these mineral (Wyborn 1983) show that 63–79 % of Re budget is hosted by the oxide minerals in gabbro samples BP3 and BP39. Although Re may partitioned more readily into sulfides than oxides, our study shows that oxides, because of their higher abundance, are the major sink for Re. Fonseca et al. (2007) showed that partitioning of Re between sulfide melt and silicate melt decreases with increasing fO_2 (Fonseca et al. 2007). The high fO_2 of the BPZP may have restricted the partitioning of Re into its sulfides.

Timing and mechanism of sulfide saturation in the BPZP magma

The sulfide blebs are found in the rims of cumulus pyroxenes or associated with mafic intercumulus minerals, which indicates that sulfide saturation occurred late relative to the growth of the cumulus minerals and that the magma was not sulfide-saturated before magma differentiation in a shallow magma chamber, although saturation must have

Table 7 PGE and Re analyses of TDB-1 (ppb)

	Ir	Rh	Pt	Pd	Re
TDB-1 (CANMET)					
#1	0.060	0.415	4.13	22.7	
#2	0.069	0.426	4.18	21.4	
#3	0.081	0.429	4.96	25.0	0.73
#4	0.083	0.408	4.81	24.2	0.81
#5	0.052	0.389	3.78	22.3	0.53
Average ($n = 5$)	0.069 ± 0.027	0.413 ± 0.032	4.37 ± 0.99	23.1 ± 2.9	0.69 ± 0.29
M&M[a] ($n = 7$)	0.075 ± 0.018	0.471 ± 0.078	5.01 ± 0.34	24.3 ± 3.4	0.79 ± 0.04
P[b] ($n = 8$)	0.078 ± 0.006		4.40 ± 0.30	24.8 ± 1.4	
Certified[c]	0.150	0.70	5.80	22.4	

Uncertainties are quoted at 2σ level

[a] Meisel and Moser (2004), high pressure asher (HPA) digestion ID-ICP-MS

[b] Peucker-Ehrenbrink et al. (2003), Ni–sulfide fire assay ID-ICP-MS

[c] Govindaraju (1994), note that Ir, Ru, and Rh values are provisional values

been imminent. This is consistent with the high abundances of PGE in the gabbro. If it were saturated with sulfide at depth or during magma ascent, the BPZP magma would have lost a majority of PGE to the segregating immiscible sulfide melts and PGE contents in the gabbro would be low. Gabbroic rocks from mafic intrusions that are considered to have formed after extensive sulfide segregation commonly contain low total PGE contents less than 3 ppb (e.g., Wang et al. 2011; Bai et al. 2012), whereas the BPZP gabbros contain 10–13 ppb total PGE.

The behavior of Cu and Pd in a sulfur-saturated magma is well understood, and Cu/Pd ratios have been regarded as a useful tool for identifying sulfide saturation in evolving magmas (e.g., Campbell and Barnes 1984; Barnes and Naldrett 1985; Vogel and Keays 1997; Philipp et al. 2001). This is because Pd partitions preferentially into sulfide melt relative to Cu ($D_{Cu}^{\text{sulfide-silicate melt}} \sim 10^3$ and $D_{Pd}^{\text{sulfide-silicate melt}} > 10^4$–$10^5$; Francis 1990; Bezmen et al. 1994; Peach et al. 1994; Ripley et al. 2002; Fonseca et al. 2009). Therefore, if a silicate melt becomes sulfide-saturated, the Cu/Pd ratio will rapidly increase. In the BPZP, Cu/Pd gradually increases from 6.1×10^3 to 5.3×10^4 as MgO content decreases (Fig. 7a). This trend implies that the variation of PGE and Cu in the BPZP is controlled by the progressive segregation of an immiscible sulfide melt. The increase is monotonic and starts from the highest MgO sample, suggesting the sulfide saturation started early in the gabbroic stage of crystallization and proceeded continuously. The low Cu/Pd ratios of the gabbros (6.1×10^3–1.4×10^4) relative to gabbroic rocks from mafic intrusions that formed after extensive sulfide segregation ($\sim 2 \times 10^4$–2×10^6; Wang et al. 2011; Bai et al. 2012) indicate that the BPZP magma did not experience sulfide saturation at depth.

Crustal contamination may have played an important role in triggering sulfide saturation in the BPZP. Isotopic evidence from δ^{18}O-εHf_i-εNd_i data and the presence of inherited zircon in the BPZP show that the BPZP magma has assimilated up to 20 % of crustal materials (Ickert 2010; Ickert et al. 2011). The assimilation of sulfur-rich sedimentary rocks and metasediments may have increased the sulfur content of the BPZP magma to near sulfide saturation; moreover, the addition of SiO_2 could have lowered the solubility of sulfide in the silicate melt (e.g., Irvine 1975).

Once the BPZP magma was emplaced into the shallow crust, it started to cool, especially at the margin of the magma chamber, crystallizing high temperature minerals such as clinopyroxene and orthopyroxene with minor ilmenite and magnetite. Crystallization of these Fe–Mg silicate and Fe-oxide minerals depleted the magma in Fe and the depletion of Fe is likely to have been most effective in the vicinity of the growing Fe-bearing minerals. Crystallization of magnetite may also have decreased oxygen fugacity because it preferentially consumes Fe^{3+} to Fe^{2+} and decrease Fe^{3+}/Fe^{2+} ratio in a melt (e.g., Jenner et al. 2010). Sulfur solubility in silicate melts is controlled by temperature, and Fe content of the melt and oxygen fugacity (Haughton et al. 1974; Mavrogenes and O'Neill 1999; O'Neill and Mavrogenes 2002; Liu et al. 2007; Jugo 2009). The combined effect of falling temperature and a decrease in the Fe content and oxygen fugacity are the probable triggers that led to sulfide saturation during the late gabbroic stage of fractionation of the BPZP. This suggestion is consistent with the occurrence of most magmatic sulfides as inclusions in the rim of cumulus pyroxene and phenocrysts, and interstitial hornblende and

biotite, commonly associated with magnetite in the gabbro (Fig. 3).

PGE variations in the BPZP

Since the onset of the sulfide saturation is during the late gabbroic stage, the concentrations of PGE in the gabbros are dominantly controlled by relative proportions of PGE-poor cumulus mineral and PGE-rich intercumulus melts in the gabbro, whereas the PGE compositions in the granodiorite, granite, and aplite reflect magma differentiation by fractionation and accumulation of immiscible cumulus sulfide blebs.

Two types of gabbros are recognized in the BPZP. The Type-1 gabbros contain more PGE, especially Pd and Pt, than the Type-2 gabbros. This difference is probably related to the abundance of intercumulus melt in the gabbros. During the formation of the gabbros by liquid–crystal fractionation, the PGE are incompatible in the cumulus pyroxene and plagioclase and concentrate in the melt. Consequently, gabbros with a high percentage of cumulus minerals and low percentage of intercumulus minerals should contain lower PGE contents than gabbros that trap a high percentage of intercumulus melt. This hypothesis is consistent with the observation that PGE-poor Type-2 gabbros have more pyroxene and plagioclase (81–85 modal %) and less intercumulus hornblende, biotite, and quartz (14–16 modal %) than Type-1 gabbros, which have 71 modal % pyroxene and plagioclase, and 27–34 modal % interstitial phases (Wyborn 1983). Type-2 gabbros are also depleted in incompatible elements such as Rb, Th, La, Ce, and Nd compared to the Type-1 gabbros at similar SiO_2 and MgO contents (Fig. 8; Table 6), showing that the Type-2 gabbro traps less intercumulus melt than Type-1. Finally, the mass balance calculations discussed earlier show that the Type-2 gabbros contain less chalcopyrite and have less Cu-rich sulfide blebs than the Type-1 gabbros (Table 1).

The granodiorite is characterized by complex isotopic data, which cannot be explained by simple closed system assimilation and fractional crystallization processes (Ickert 2010). This isotopic heterogeneity in the granodiorite suggests that it formed from several pulses of magma that were contaminated by varying amounts of continental crustal materials (Ickert 2010). Although crustal assimilation significantly disturbed isotopic characteristics of the granodiorites (Ickert 2010) because of the relatively large contrast of contaminant endmember composition with the magma, its influence on PGE geochemistry is likely to be minor because PGE contents in the crustal rocks are very low (Park et al. 2012b) and the degree of assimilation is small (10–20 %; Ickert 2010).

The granodiorite contains Pd and Pt at concentration levels comparable to those in the gabbro but it is

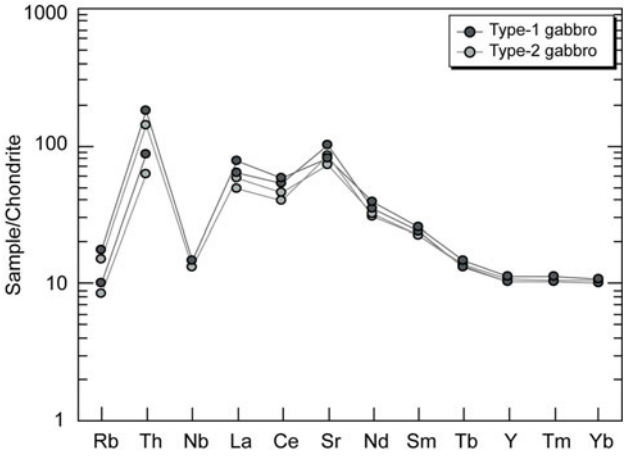

Fig. 8 Chondrite-normalized trace elements for the gabbro. Normalizing values from Sun and McDonough (1989)

significantly depleted in Rh and Ir so that the granodiorite has a high Pd/Ir relative to the gabbro. From this we infer that the magma of the granodiorite may have experienced Ir-rich alloy fractional crystallization, which fractionates Ir from Pd. Sulfide segregation and distribution cannot produce such difference between the granodiorite and the gabbro because all PGE have a similar affinity for immiscible sulfide melts (Bezmen et al. 1994; Peach et al. 1994).

Duplicate analyses of some gabbro and granodiorite samples show variations that lie well outside analytical error, which may reflect a nugget effect (Fig. 5). The problem is especially apparent for Ir, which shows large variations relative to other PGE in the gabbro and the granodiorite, suggesting presence of an Ir-rich alloy during the early stages of crystallization of the BPZP. Once sulfide saturation was established, it would have lowered the Ir content of the melt below that required for Ir saturation and, as a consequence, the Ir-rich alloy is unlikely to have persisted beyond the late gabbroic stages of the magma evolution. The Ir-rich alloy would have sequestered some of the other PGE, but to a lesser extent. A number of studies (Barnes et al. 1985; Peck et al. 1992; Philipp et al. 2001; Momme et al. 2002; Barnes and Fiorentini 2008; Pitcher et al. 2009; Ireland et al. 2009) have suggested that an Ir-rich alloy may host PGE in ultramafic–mafic magmas. The Ir-rich alloy may have been entrapped in co-crystallizing phenocrysts or cumulus phases and accumulated in the gabbro and the granodiorite, producing the observed nugget effect.

The PGE variations in the granite and the aplite show typical trends of a sulfide-saturated magma with all of these elements having positive correlations with MgO (Fig. 5). However, the magma that formed the granite cannot be the same as the one that formed the granodiorite because overall trends of Ni, Rh, and Ir within granodiorite and

granite are not continuous and Ir content in the granite is significantly higher than that of most of the granodiorites (Fig. 5). Furthermore, the cross-cutting relationship between the granite and granodiorite (Fig. 1), which differs from the gradual contact between the gabbro and granodiorite, as well as homogeneous isotopic signature of the granite, suggests the input of a new batch of magma into the magma chamber after the nearly complete solidification of the granodiorite (Ickert 2010). The low PGE content and low Pd/Ir ratio of the granite indicate that the magma from which the granites formed experienced sulfide saturation at depth and was not involved with the processes that fractionated Pd from Ir such as fractionation of Ir-rich alloy. Duplicate analyses of a granite sample (BP19-I and BP19-II) show significant heterogeneity in all PGE (Fig. 5), which we attribute to sulfide nuggets. This variation cannot be due to an Ir-rich alloy because it also affects the other PGE including Pd which does not partition into a metal alloy (e.g., Barnes and Fiorentini 2008; Park et al. 2012a).

Implications to exploration of Cu–Au ore deposits associated with felsic magmatic systems

The sulfide data, mass balance calculations, and Cu and PGE geochemistry of the BPZP show that sulfide saturation occurred at the late gabbroic stage of magma differentiation and that segregation of an immiscible sulfide melt controlled Cu and PGE variations within the pluton, with silicate and oxide mineral fractionation having little effect. The sulfide melt sequestered a significant portion of the magmatic Cu and PGE, and probably Au, locking them in the cumulate rocks and restricting the availability of these metals to ore-forming fluids. Therefore, we suggest that the roof rocks that overlay the BPZP were not prospective for magmatic-hydrothermal Cu, Au, or Cu–Au deposits.

The key to distinguish felsic intrusions that give rise to Cu–Au magmatic-hydrothermal deposits from barren ones that do not is to identify the onset of sulfide saturation during the evolution of the intrusion. The BPZP provides an example of the behavior of Cu and PGE in a barren felsic system. A decrease of Cu and PGE, associated with an increase in Cu/Pd, indicates sulfide saturation and can be applied to all rock types including felsic rocks. Alternatively, in a productive felsic system associated with Cu–Au mineralization, the Cu/Pd and Au/Pd ratios of the residual magma are expected to decrease when the magma becomes saturated with a magmatic fluid because experimental and thermodynamic studies showed that Cu and Au have stronger affinity to magmatic fluid than PGE under the same fluid conditions (Wood 1987; Simon et al. 2006; Simon and Pettke 2009). In addition, the various PGE are also expected to partition differently into the magmatic fluid according to the nature of the fluid phase and the fO_2 of the melt (Hanley et al. 2005). Setiabudi et al. (2007) investigated PGE, Re, and Au geochemistry of andesitic intrusions of the Kelian Region, Indonesia, which are associated with the Kelian Au deposit. They found that a systematic depletion in Au relative to adjacent PGE on a mantle-normalized diagram and suggested that a magmatic fluid preferentially stripped Au from the crystallizing magma to form the Au ore deposit. More studies on Cu, Au, and PGE geochemistry of productive felsic intrusions are required in order to evaluate the use of these elements as a tool for distinguishing barren felsic suites from productive felsic suites.

Conclusions

The BPZP provides an example of behavior of Cu and PGE in a sulfide-saturated barren compositionally diverse magmatic system. Whole rock Cu and PGE concentrations decrease and the Cu/Pd ratios increase with decreasing MgO contents. These variations are mainly controlled by the segregation and distribution of magmatic sulfide blebs, with silicate and oxide minerals accounting for less than 13 % of the budget of these elements. Sulfide saturation started during the late gabbroic stage of magma evolution in the shallow magma chamber that host the BPZP rocks as a consequence of a combination of decreasing temperature, iron content, and oxygen fugacity, whereas the magma from which the granites formed experienced initial sulfide saturation at depth. The discontinuities in the trends for Ni, Rh, Ir, and Pd/Ir ratio against MgO occur at the contacts between rock types and are attributed to the entry of new pulses of magma into the chamber. The granodiorites, and to a lesser extent the gabbros, experienced fractionation of Ir-rich alloy, whereas the granites were not involved with the process. Early sulfide saturation depleted the BPZP magma in all chalcophile elements, which resulted in a barren magmatic system that could not produce Cu–Au hydrothermal deposits.

Acknowledgments This research was funded by an ARC Discovery Grant to Ian Campbell. We thank Bruce Chappell, Doone Wyborn, Ian Williams, and Keith Sircombe for their help in collecting the BPZP samples. We also thank Read Keays for his constructive comments and Jochen Hoefs for his efficient editorial handling.

References

Bai ZJ, Zhong H, Naldrett AJ, Zhu WG, Xu GW (2012) Whole-rock and mineral composition constraints on the genesis of the Giant Hongge Fe-Ti-V oxide deposit in the Emeishan Large Igneous Province, Southwest China. Econ Geol 107:507–524

Barnes SJ, Fiorentini ML (2008) Iridium, ruthenium and rhodium in komatiites: evidence for iridium alloy saturation. Chem Geol 257:44–58

Barnes SJ, Naldrett AJ (1985) The fractionation of the platinum-group elements at the Alexo Komatiite, Abitibi Greenstone-Belt, Northern Ontario. Can Mineral 23:295

Barnes SJ, Naldrett AJ, Gorton MP (1985) The origin of the fractionation of platinum-group elements in terrestrial magmas. Chem Geol 53:303–323

Barnes S-J, Cox RA, Zientek ML (2006) Platinum-group element, gold, silver and base metal distribution in compositionally zoned sulfide droplets from the Medvezky Creek Mine, Noril'sk, Russia. Contrib Mineral Petrol 152:187–200

Barnes SJ, Prichard HM, Cox RA, Fisher PC, Godel B (2008) The location of the chalcophile and siderophile elements in platinum-group element ore deposits (a textural, microbeam and whole rock geochemical study): implications for the fort-nation of the deposits. Chem Geol 248:295–317

Bezmen NI, Asif M, Brügmann GE, Romanenko IM, Naldrett AJ (1994) Distribution of Pd, Rh, Ru, Ir, Os, and Au between sulfide and silicate metals. Geochim Cosmochim Acta 58:1251–1260

Campbell IH (2003) Constraints on continental growth models from Nb/U ratios in the 3.5 Ga barberton and other Archaean basalt-komatiite suites. Am J Sci 303:319–351

Campbell IH, Barnes SJ (1984) A model for the geochemistry of the platinum-group elements in magmatic sulfide deposits. Can Mineral 22:151–160

Candela PA (1997) A review of shallow, ore-related granites: textures, volatiles, and ore metals. J Petrol 38:1619–1633

Carmichael ISE (1966) The iron-titanium oxides of salic volcanic rocks and their associated ferromagnesian silicates. Contrib Mineral Petrol 14:36–64

Carroll MR, Rutherford MJ (1985) Sulfide and sulfate saturation in hydrous silicate melts. J Geophys Res 90:C601–C612

Crocket JH (2000) PGE in fresh basalt, hydrothermal alteration products, and volcanic incrustations of Kilauea volcano, Hawaii. Geochim Cosmochim Acta 64:1791–1807

Crocket JH, Fleet ME, Stone WE (1997) Implications of composition for experimental partitioning of platinum-group elements and gold between sulfide liquid and basalt melt: the significance of nickel content. Geochim Cosmochim Acta 61:4139–4149

Dare SAS, Barnes S-J, Prichard HM (2010) The distribution of platinum group elements (PGE) and other chalcophile elements among sulfides from the Creighton Ni-Cu-PGE sulfide deposit, Sudbury, Canada, and the origin of palladium in pentlandite. Miner Deposita 45:765–793

Dare S, Barnes S-J, Prichard H, Fisher P (2011) Chalcophile and platinum-group element (PGE) concentrations in the sulfide minerals from the McCreedy East deposit, Sudbury, Canada, and the origin of PGE in pyrite. Miner Deposita 46:381–407. doi: 10.1007/s00126-011-0336-9

Ebel DS, Naldrett AJ (1997) Crystallization of sulfide liquids and the interpretation of ore composition. Can J Earth Sci 34:352–365

Fonseca ROC (2007) The high-temperature geochemistry of the highly siderophile elements, Pt, Re, Ir, Os and Rh. The Australian National University, Canberra

Fonseca ROC, Mallmann G, O'Neill HSC, Campbell IH (2007) How chalcophile is rhenium? An experimental study of the solubility of Re in sulphide mattes. Earth Planet Sci Lett 260:537–548

Fonseca ROC, Campbell IH, O'Neill HSC, Allen CM (2009) Solubility of Pt in sulphide mattes: implications for the genesis of PGE-rich horizons in layered intrusions. Geochim Cosmochim Acta 73:5764–5777

Francis RD (1990) Sulfide globules in midocean ridge basalts (Morb), and the effect of oxygen abundance in Fe-S-O liquids on the ability of those liquids to partition metals from Morb and Komatiite magmas. Chem Geol 85:199–213

Gao S, Liu XM, Yuan HL, Hattendorf B, Gunther D, Chen L, Hu SH (2002) Determination of forty two major and trace elements in USGS and NIST SRM glasses by laser ablation-inductively coupled plasma-mass spectrometry. Geostandard Newslett 26:181–196

Glen RA (2005) The Tasmanides of eastern Australia. In: Naughan APN, Leat PT (eds) Terrane processes at the margins of Gondwana, vol 246. The Geological Society of London, London, pp 23–96

Govindaraju K (1994) 1994 Compilation of working values and sample description for 383 geostandards. Geostandards Newsl 18:331–334

Hanley JJ, Pettke T, Mungall JE, Spooner ETC (2005) The solubility of platinum and gold in NaCl brines at 1.5 kbar, 600 to 800 degrees C: a laser ablation ICP-MS pilot study of synthetic fluid inclusions. Geochim Cosmochim Acta 69:2593–2611

Haughton DR, Roeder PL, Skinner BJ (1974) Solubility of sulfur in mafic magmas. Econ Geol 69:451–467

Hoskin PWO (2000) Patterns of chaos: fractal statistics and the oscillatory chemistry of zircon. Geochim Cosmochim Acta 64: 1905–1923

Hoskin PWO, Kinny PD, Wyborn D, Chappell BW (2000) Identifying accessory mineral saturation during differentiation in granitoid magmas: an integrated approach. J Petrol 41:1365–1396

Ickert RB (2010) U-Pb, Lu-Hf, and O isotope systematics of zircon from southeastern Australian Siluro-Devonian granites. The Australian National University, Canberra

Ickert RB, Williams IS, Wyborn D (2011) Ti in zircon from the Boggy Plain zoned pluton: implications for zircon petrology and Hadean tectonics. Contrib Mineral Petrol 162:447–461

Ireland TJ, Walker RJ, Garcia MO (2009) Highly siderophile element and Os-187 isotope systematics of Hawaiian picrites: implications for parental melt composition and source heterogeneity. Chem Geol 260:112–128

Irvine TN (1975) Crystallization sequences in the Muskox intrusion and other layered intrusions-II. Origin of chromitite layers and similar deposits of other magmatic ores. Geochim Cosmochim Acta 39:991–1008

Jenner FE, O'Neill HSC, Arculus RJ, Mavrogenes JA (2010) The magnetite crisis in the evolution of arc-related magmas and the initial concentration of Au, Ag and Cu. J Petrol 51:2445–2464

Jugo PJ (2009) Sulfur content at sulfide saturation in oxidized magmas. Geology 37:415–418

Keith JD, Whitney JA, Hattori K, Ballantyne GH, Christiansen EH, Barr DL, Cannan TM, Hook CJ (1997) The role of magmatic sulfides and mafic alkaline magmas in the Bingham and Tintic mining districts, Utah. J Petrol 38:1679–1690

Larocque ACL, Stimac JA, Keith JD, Huminicki MAE (2000) Evidence for open-system behavior in immiscible Fe-S-O liquids in silicate magmas: implications for contributions of metals and sulfur to ore-forming fluids. Can Mineral 38:1233–1249

Liu YN, Samaha NT, Baker DR (2007) Sulfur concentration at sulfide saturation (SCSS) in magmatic silicate melts. Geochim Cosmochim Acta 71:1783–1799

Longerich HP, Jackson SE, Gunther D (1996) Laser ablation inductively coupled plasma mass spectrometric transient signal data acquisition and analyte concentration calculation. J Anal Atom Spectrom 11:899–904

Mavrogenes JA, O'Neill HSC (1999) The relative effects of pressure, temperature and oxygen fugacity on the solubility of sulfide in mafic magmas. Geochim Cosmochim Acta 63:1173–1180

McDonough WF, Sun SS (1995) The composition of the earth. Chem Geol 120:223–253

Meisel T, Moser J (2004) Platinum-group element and rhenium concentrations in low abundance reference materials. Geostand Geoanal Res 28:233–250

Meisel T, Fellner N, Moser J (2003) A simple procedure for the determination of platinum group elements and rhenium (Ru, Rh,

Pd, Re, Os Ir and Pt) using ID-ICP-MS with an inexpensive on-line matrix separation in geological and environmental materials. J Anal Atom Spectrom 18:1318

Momme P, Tegner C, Brooks CK, Keays RR (2002) The behaviour of platinum-group elements in basalts from the East Greenland rifted margin. Contrib Mineral Petrol 143:133–153

O'Neill HSC, Mavrogenes JA (2002) The sulfide capacity and the sulfur content at sulfide saturation of silicate melts at 1400 degrees C and 1 bar. J Petrol 43:1049–1087

Park J-W, Campbell IH, Eggins SM (2012a) Enrichment of Rh, Ru, Ir and Os in Cr spinels from oxidized magmas: evidence from the Ambae volcano, Vanuatu. Geochim Cosmochim Acta 78:28–50

Park J-W, Hu Z, Gao S, Campbell IH, Gong H (2012b) Platinum group element abundances in the upper continental crust revisited—new constraints from analyses of Chinese loess. Geochim Cosmochim Acta 93:63–76

Paster TP, Schauwecker DS, Haskin LA (1974) The behavior of some trace elements during solidification of the Skaergaard layered series. Geochim Cosmochim Acta 38:1549–1577

Peach CL, Mathez EA, Keays RR, Reeves SJ (1994) Experimentally determined sulfide melt-silicate melt partition-coefficients for iridium and palladium. Chem Geol 117:361–377

Peck DC, Keays RR, Ford RJ (1992) Direct crystallization of refractory platinum-group element alloys from primitive magmas: evidence from Western Tasmania. Aust J Earth Sci 39:373–387

Peucker-Ehrenbrink B, Bach W, Hart SR, Blusztajn JS, Abbruzzese T (2003) Rhenium-osmium isotope systematics and platinum group element concentrations in oceanic crust from DSDP/ODP Sites 504 and 417/418. Geochem Geophys Geosyst 4:2002GC000414

Philipp H, Eckhardt JD, Puchelt H (2001) Platinum-group elements (PGE) in basalts of the seaward-dipping reflector sequence, SE Greenland coast. J Petrol 42:407–432

Pitcher L, Helz RT, Walker RJ, Piccoli P (2009) Fractionation of the platinum-group elements and Re during crystallization of basalt in Kilauea Iki Lava Lake. Hawaii. Chem Geol 260:196–210

Ripley EM, Brophy JG, Li CS (2002) Copper solubility in a basaltic melt and sulfide liquid/silicate melt partition coefficients of Cu and Fe. Geochim Cosmochim Acta 66:2791–2800

Robb LJ (2004) Introduction to ore-forming processes. Blackwell, Oxford

Setiabudi BT, Campbell IH, Martin CE, Allen CM (2007) Platinum group element geochemistry of andesite intrusions of the Kelian region, East Kalimantan, Indonesia: implications of gold depletion in the intrusions associated with the Kelian gold deposit. Econ Geol 102:95–108

Simon AC, Pettke T (2009) Platinum solubility and partitioning in a felsic melt-vapor-brine assemblage. Geochim Cosmochim Acta 73:438–454

Simon AC, Pettke T, Candela PA, Piccolli PM, Heinrich CA (2006) Copper partitioning in a melt-vapor-brine-magnetite-pyrrhotite assemblage. Geochim Cosmochim Acta 70:5583–5600

Stavast WJA, Keith JD, Christiansen EH, Dorais MJ, Tingey D, Larocque A, Evans N (2006) The fate of magmatic sulfides during intrusion or eruption, Bingham and Tintic districts, Utah. Econ Geol 101:329–345

Sun SS, McDonough WF (1989) Chemical and isotopic systematics of oceanic basalts: implications for mantle composition and processes. In: Saunders AD, Norry MJ (eds) Magmatism in the Ocean Basins, vol 42. Geological Society of London, London

Sylvester PJ, Eggins SM (1997) Analysis of Re, Au, Pd, Pt and Rh in NIST glass certified reference materials and natural basalt glasses by laser ablation ICP-MS. Geostandard Newsl 21:215–229

Tomkins AG (2010) Wetting facilitates late-stage segregation of precious metal-enriched sulfosalt melt in magmatic sulfide systems. Geology 38:951–954

Vogel DC, Keays RR (1997) The petrogenesis and platinum-group element geochemistry of the Newer Volcanic Province, Victoria, Australia. Chem Geol 136:181–204

Wang CY, Zhou MF, Qi L (2011) Chalcophile element geochemistry and petrogenesis of high-Ti and low-Ti magmas in the Permian Emeishan large igneous province, SW China. Contrib Mineral Petrol 161:237–254

Wood SA (1987) Thermodynamic calculations of the volatility of the platinum group elements (Pge)—the Pge content of fluids at magmatic temperatures. Geochim Cosmochim Acta 51:3041–3050

Wyborn D (1983) Fractionation processes in the Boggy Plain zoned pluton. The Australian National University, Canberra

Wyborn D, Turner BS, Chappell BW (1987) The Boggy plain Supersuite—a distinctive belt of I-type igneous rocks of potential economic-significance in the Lachlan fold belt. Aust J Earth Sci 34:21–43

Wyborn D, Chappell BW, James M (2001) Examples of convective fractionation in high-temperature granites from the Lachlan Fold Belt. Aust J Earth Sci 48:531–541